Acoustic modes of locally resonant phononic crystals: Comparison with frequency-dependent mass models

Kenny L. S. Yip[*] and Sajeev John[†]
Department of Physics, University of Toronto, 60 St. George Street, Toronto, Ontario, Canada M5S 1A7

(Received 6 November 2020; revised 7 March 2021; accepted 10 March 2021; published 18 March 2021)

Locally resonant acoustic materials were proposed to control sound using structures with feature size orders of magnitude smaller than the acoustic wavelength in air. We analytically derive the effective, frequency-dependent mass densities of resonant oscillators consisting of a heavy mass within a light shell, embedded in foam, in two dimensions, using a rigid core-shell approximation. The effective mass is expressible in closed form by elementary functions, enabling a mapping of the low-frequency physics to a simple one-dimensional model involving a point mass harmonically coupled within a box. The acoustic band structure of a two-dimensional square lattice of these oscillators is evaluated in the effective, frequency-dependent mass density model and compared with the exact solution. For the out-of-plane oscillation within this two-dimensional phononic crystal, the nonlinear eigenvalue equation resulting from the frequency-dependent density is solved with the Cutting Surface Method to yield the acoustic band structure. This agrees with the exact band structure obtained by finite element method calculations within 2% numerical error. For the in-plane oscillations involving internal translations or rotations within the core-shell resonators, the one-dimensional mass-in-a-box model recaptures the exact acoustic modes at only certain high-symmetry points of the two-dimensional Brillouin zone. The description of more complex resonances within acoustic metamaterials requires a fundamental generalization of current effective mass models.

DOI: 10.1103/PhysRevB.103.094304

I. INTRODUCTION

Considerable research has been focused on the behavior of electromagnetic waves in photonic crystals designed with photonic band gaps, within which light can be localized [1,2]. These periodic dielectric structures exhibit a variety of unprecedented physical properties. An excited atom in the band gap of a photonic crystal is locked in the excited state by inhibition of photon spontaneous emission to form an atom-photon bound state [3]. Even in the absence of a photonic band gap, "slow-light" modes enable novel light-trapping effects, with applications such as high-efficiency solar energy harvesting in thin films [4]. In the case of acoustic materials, localization of high-frequency phonons can be realized in a disordered elastic medium [5,6]. Motivated by the advances in photonic crystals, attention has turned to acoustic crystals consisting of periodic arrays of elastic materials designed to exhibit phononic band gaps [7,8]. Early theoretical work focused on the existence of acoustic band gaps in specific two-dimensional arrays of elastic materials. The pioneering work of Kushwaha consisted of a square lattice of parallel circular nickel rods embedded in an aluminum background [7]. Experimentally, absolute ultrasonic band gaps were confirmed in various millimeter-sized, two-dimensional, periodic, binary composites, including a square lattice of mercury circular cylinders in an aluminum alloy matrix [9] and a triangular lattice of steel circular cylinders in an epoxy matrix [10]. Acoustic band gaps over the audible frequency range were achieved with bulky meter-sized composites [11]. Conventional composite of elastic materials suffer from the requirement for very large feature sizes to be effective in controlling sound over the audible frequency range. The wavelength of the standard 440 Hz tuning pitch is about 0.78 m in air and 14 m in solid steel [12]. Conventional phononic crystals, sensitive to the audible frequency range, typically consist of repeating unit cells of size comparable to the sound wavelength. This "scaling problem" presents an impractical situation for many real-world applications.

To overcome the scaling problem, Liu *et al.* proposed locally resonant sonic materials composed of dense, stiff lead balls coated by light, elastic, silicone rubber. Using a lattice constant of only 1.55 cm, they achieved an acoustic band gap in the audible range from 400 Hz to 600 Hz [13]. An analytical explanation was provided based on the local resonance and a resulting negative effective mass density [14]. Subsequent work extended the concept of locally resonant oscillators to potential applications, such as acoustic cloaking [15], negative refraction, and subdiffraction-limit resolution [16]. While the idea of local resonance is valuable, the derivation of an effective frequency-dependent mass density by Liu *et al.* offers little physical intuition and involves implicit inversion of four-by-four matrices [14].

In this paper, we calculate the acoustic modes of a two-dimensional locally resonant phononic crystal with a lattice constant of 1 cm, consisting of a dense steel cylindrical core,

[*]Author to whom correspondence should be addressed: lskyip@physics.utoronto.ca
[†]john@physics.utoronto.ca

 ©2021 American Physical Society

encapsulated by a coaxial rigid cellulose cylindrical shell and surrounded by soft open-cell foam. Open-cell foam is commonly used for the control of sound in household and industrial applications. Cellulose nitrate and stainless steel are chosen as the inertial components of the resonators for the ease of availability and machinability. This choice of materials allows important features, such as band gaps and flat bands, to appear at audible frequencies in a phononic crystal with small, centimeter-sized lattice constant. Such features may be useful for reflecting or absorbing sound in relatively thin sheets. Moreover, these materials are less toxic than mercury [9] and lead [13] described in previous literature.

In our two-dimensional structure (with translational invariance in the axial direction), the transverse out-of-plane modes are decoupled from the in-plane modes. As shown below, the sub-wavelength out-of-plane acoustic band structure consists of two bands in the audible frequency range, with the lower band and upper band corresponding to in-phase and antiphase translational motions, respectively, between the steel core and the cellulose shell.

We derive a closed form, frequency-dependent, effective mass model for the out-of-plane motion using a rigid core-shell approximation (RCSA). The out-of-plane acoustic band structure, obtained by solving a nonlinear eigenvalue equation, agrees (within 2% error) with the bands of the true structure, obtained by finite element method. On the other hand, the in-plane motion consists of six resonant modes, associated with the in-phase and antiphase relative translations (in two orthogonal directions) and relative rotations of the core and shell. For the in-plane acoustic band structure, the three in-phase and the three antiphase bands in the audible frequency range are separated by an acoustic band gap. The intricate coupling between the rotational and translational resonances leads to insufficiency of the simple frequency-dependent effective mass density model. A nontrivial generalization of this model is required to account for the in-plane acoustic band structure at all wave vectors.

We summarize, below, certain unique aspects of this work. Unlike previous literature, our paper provides an exact analytical treatment and derivation of the effective frequency-dependent mass of the resonator by elastostatic analysis. We apply the frequency-dependent, effective mass to calculate the acoustic band structure with a powerful Cutting Surface Method (CSM) [17]. This technique provides exact band structure in the presence of frequency-dependent mass densities and elastic parameters. We establish the effectiveness of CSM to solve nonlinear eigenvalue problems in the context of acoustics. We also resolve, in Appendix A, a long-standing convergence issue [8,18,19] of plane wave expansions for acoustic band structure calculations [20–22]. Our paper goes beyond the rudimentary concept of a single frequency-dependent, effective mass and reveals the requirement for an independent frequency-dependent moment of inertia to recapture phononic bands involving rotational modes of the resonators. Our calculations provide physical insight into the frequency range over which the frequency-dependent mass model applies. This is connected to the elastostatic treatment of the interior of each resonator, which breaks down at high frequencies where wavelike deformations of a single resonator may occur. Our paper precisely delineates the circumstances under which the simple frequency-dependent effective mass model fails both conceptually and numerically. This occurs in the case of unit cells with multiple resonances where one type of resonance can excite another type of resonance in a nearby unit cell. This is an essential backdrop for future research to go beyond the simple effective mass model. It lays the groundwork for a more fundamental physical picture that can encompass multiple resonant modes of a individual resonators and their couplings to nearby resonators.

Our effective mass treatment is distinct from the previous homogenization approaches. In conventional homogenization, the effective mass densities are often empirically determined, *posteriori*, assuming knowledge of the transmission spectrum [13] or the acoustic band structure [19,23]. In contrast, our effective masses are determined analytically by linear elasticity, *a priori*. The acoustic band structure follows from the frequency-dependent, effective mass by solving an underlying nonlinear eigenvalue equation. Our effective masses are expressible in terms of closed-form rational functions in frequency, providing physical insights into the origin of the local resonance and its precise frequency dependence. Unlike conventional homogenization, where the entire composite is approximated as an effective medium [19,23–26], in our effective mass models, only the local resonantor is replaced by a frequency-dependent density.

This article is organized as follows. In Sec. II we review the concept of frequency-dependent, effective mass with a simple one-dimensional mass-in-a-box model. We also introduce our centimeter-sized resonant unit composed of steel cores surrounded by cellulose shells embedded in open-cell foam. This is complemented with a brief discussion of linear elasticity, plane wave expansion and numerical convergence. In Sec. III we derive the three different frequency-dependent, effective mass densities for out-of-plane oscillation and in-plane translational and rotational oscillations using our proposed RCSA. In Sec. IV we apply our analytically derived, out-of-plane, frequency-dependent, effective mass density, and solve the associated nonlinear eigenvalue problem with the Cutting Surface Method (CSM) [17]. We then compare the results of the effective mass model with the band structure of the true material obtained by finite element method. In Sec. V we discuss limitations of the simple frequency-dependent effective density models arising from the coupling between in-plane translational and rotational resonances. In Appendix A, we discuss the convergence of acoustic plane wave expansions in the presence of material discontinuities. In Appendix B, algebraic details of the RCSA calculations of in-plane translational modes are presented. Similarly, in Appendix C, details of the RCSA calculations of in-plane rotational modes are provided.

II. MODEL OF A LOCALLY RESONANT PHONONIC CRYSTAL

The concept of frequency-dependent, effective mass is outlined with a one-dimensional harmonic oscillator model of a point mass within a rigid box [27]. The physical resonant oscillator consists of a centimeter-sized unit composed of a dense steel core, surrounded by soft open-cell foam encapsulated by a stiff cellulose shell. In the effective mass picture,

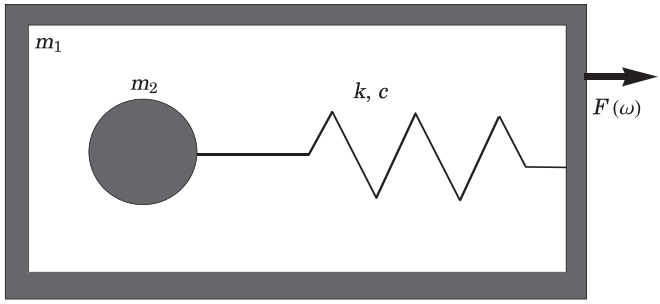

FIG. 1. A rigid box of mass, m_1, subject to a harmonic force, $F(\omega)$, is coupled to an interior point mass, m_2, by a dissipative elastic spring of spring constant k and damping parameter c.

this entire resonant unit is replaced by a unit with spatially uniform, frequency-dependent mass density chosen to recapture the oscillation modes of the true phononic crystal. The plane wave expansion method for calculating acoustic band structure is briefly reviewed for our system involving products of Fourier series with complementary jump discontinuities.

A. One-dimensional mass-in-a-box model

The concept of dynamic effective mass density in a spring-mass model to represent an elastic medium with local resonances was introduced previously [27]. This concept was applied to explain the almost complete reflection of sound at frequencies where the effective dynamical mass is negative, in membrane-type acoustic metamaterials [28]. We briefly review the frequency-dependent mass model for a rigid box of mass m_1 with displacement x_1, containing a point mass m_2 with displacement x_2 held by a spring with stiffness constant k and dissipation parameter c, responding to an external harmonic force $F(\omega)$. The model is schematically shown in Fig. 1. This response is governed by the equations of motion:

$$m_1\ddot{x}_1 = F(\omega) + k(x_2 - x_1) + c(\dot{x}_2 - \dot{x}_1), \tag{1}$$

$$m_2\ddot{x}_2 = k(x_1 - x_2) + c(\dot{x}_1 - \dot{x}_2). \tag{2}$$

We show below that under the RCSA, the low-frequency dynamical response of the steel core and the cellulose shell in the true resonant acoustic structure can be analytically mapped to certain one-dimensional mass-in-a-box models. We then delineate the range of acoustic modes where the simplified frequency-dependent, effective mass models provide a faithful representation of the true modes of the original phononic crystal.

We introduce the natural frequency $\omega_0 = \sqrt{k/m_2}$ and dimensionless damping ratio $\xi = c/(2\sqrt{km_2})$. Under the external harmonic force, $F(\omega)$, both masses oscillate at the same frequency ω. Using the equation of motion (2), the displacement of the mass in the core is proportional to that of the box:

$$x_2 = \left[\frac{\omega_0^2 - 2i\xi\omega_0\omega}{\left(\omega_0^2 - \omega^2\right) - 2i\xi\omega_0\omega}\right]x_1. \tag{3}$$

For small damping ($\xi \ll 1$), at a frequency slightly above the natural frequency ($\omega \gtrsim \omega_0$), the internal mass exhibits large-amplitude, out-of-phase motion relative to the box in

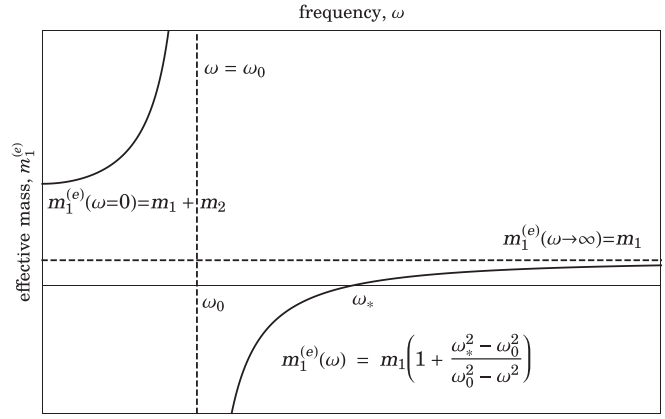

FIG. 2. Nondissipative effective frequency-dependent mass in Eq. (6) is schematically plotted. Note that the effective mass diverges at $\omega = \omega_0$, and is negative over the range $\omega_0 < \omega < \omega_*$.

which it is contained. The system of coupled differential equations could be simplified into a single variable equation by substituting the proportionality equation (3) into the equation of motion of the box (1):

$$\left[m_1 + \frac{m_2\omega_0^2 - 2i\xi m_2\omega_0\omega}{\left(\omega_0^2 - \omega^2\right) - 2i\xi\omega\omega_0}\right]\ddot{x}_1 = F(\omega). \tag{4}$$

The coefficient of the second-time derivative of the displacement could be interpreted as an *effective, frequency-dependent mass*, $m_1^{(e)}(\omega)$:

$$m_1^{(e)}(\omega) = m_1 + \frac{m_2\omega_0^2 - 2i\xi m_2\omega_0\omega}{\left(\omega_0^2 - \omega^2\right) - 2i\xi\omega\omega_0}, \tag{5}$$

so that the equation of motion assumes the form of Newton's second law: $m_1^{(e)}(\omega)\ddot{x}_1 = F(\omega)$. For small damping ($\xi \ll 1$), at a frequency slightly above the natural frequency ($\omega \gtrsim \omega_0$), the acceleration of the box may be opposite to the force. This may be interpreted as a negative effective mass of the resonant unit. For the time being, we consider nondissipative systems ($\xi = 0$), and the effective mass simplifies to

$$m_1^{(e)}(\omega) = m_1 + \frac{m_2\omega_0^2}{\omega_0^2 - \omega^2}. \tag{6}$$

This is plotted as a function of frequency in Fig. 2 with salient features outlined below.

(1) In the low-frequency limit, the two masses oscillate in phase with the same amplitude, so that the effective mass becomes the total mass of the resonant unit:

$$x_2(\omega \to 0) = \lim_{\omega\to 0}\left(\frac{\omega_0^2}{\omega_0^2 - \omega^2}\right)x_1 = x_1, \tag{7}$$

$$m_1^{(e)}(\omega \to 0) = \lim_{\omega\to 0} m_1 + \frac{m_2\omega_0^2}{\omega_0^2 - \omega^2} = m_1 + m_2. \tag{8}$$

(2) The effective mass has a simple pole at the natural frequency $\omega = \omega_0$ of the internal mass. The effective mass is positive over the range $0 < \omega < \omega_0$, and increases from the total mass in the zero-frequency limit to infinity at the internal

resonance frequency:

$$m_1^{(e)}(\omega) = m_1 + \left(\frac{m_2\omega_0^2}{\omega_0+\omega}\right)\frac{1}{\omega_0-\omega}. \tag{9}$$

(3) Setting $m_1^{(e)}(\omega_*) = 0$, we obtain the frequency, ω_*, at which the effective mass vanishes:

$$\omega_* = \sqrt{\frac{k}{m_1}+\frac{k}{m_2}} = \sqrt{\frac{k}{m_r}}, \tag{10}$$

where $m_r = (1/m_1 + 1/m_2)^{-1}$ is the reduced mass.

(4) The effective mass is negative over the range $\omega_0 < \omega < \omega_*$, and is positive beyond the zero-density frequency $\omega_* < \omega$. When expressed in terms of the zero-density frequency, the sign of the effective density is more readily observed:

$$m_1^{(e)}(\omega) = m_1\left(1+\frac{\omega_*^2-\omega_0^2}{\omega_0^2-\omega^2}\right). \tag{11}$$

When the effective mass is negative, the box oscillates in antiphase with the core mass, and the inertial response is dominated by the core oscillating at a π-phase difference. Wave propagation is inhibited over this frequency range. We show below that this is associated with a phononic band gap.

(5) In the high-frequency limit, the effect of the core mass m_2 is negligible, and the effective mass asymptotically approaches the mass of the shell. Physically, when the box oscillates rapidly, the core mass remains almost stationary by inertia:

$$m_1^{(e)}(\omega\to\infty) = \lim_{\omega\to\infty} m_1 + \frac{m_2\omega_0^2}{\omega_0^2-\omega^2} = m_1. \tag{12}$$

B. Linear elasticity

For each infinitesimal parcel of an elastic material at position $\mathbf{r} = (x_1, x_2, x_3)$, the distortion is characterized by the symmetric strain tensor ϵ_{ij} [29]:

$$\epsilon_{ij} = \frac{1}{2}\left(\frac{\partial u_i}{\partial x_j}+\frac{\partial u_j}{\partial x_i}+\frac{\partial u_k}{\partial x_i}\frac{\partial u_k}{\partial x_j}\right), \tag{13}$$

where the displacement field is denoted by $\mathbf{u} = (u_1, u_2, u_3)$. Einstein summation convention, where repeated indices are summed over, is assumed throughout this article. For small displacement, the strain tensor is approximated by the linearized form:

$$\epsilon_{ij} = \frac{1}{2}\left(\frac{\partial u_i}{\partial x_j}+\frac{\partial u_j}{\partial x_i}\right). \tag{14}$$

Elastic restoring stress arises from the strain, and the general linear relation between the stress tensor σ_{ij} and the strain tensor ϵ_{ij} is given by

$$\sigma_{ij} = C_{ijkl}\epsilon_{kl}, \tag{15}$$

where $\mathbf{C}$ is a fourth-order stiffness tensor with at most 21 independent material constants due to symmetries of the strain and stress tensors. In isotropic linear elastic materials, there are only two free material constants, namely, the Lamé coefficient of bulk deformation λ associated with volume change, and the Lamé coefficient of shear deformation μ associated with lateral distortion. In this case, the constitutive relation simplifies to [29]

$$\sigma_{ij} = (\lambda\delta_{ij}\delta_{kl} + 2\mu\delta_{ik}\delta_{jl})\epsilon_{kl} = \lambda\epsilon_{kk}\delta_{ij} + 2\mu\epsilon_{ij}, \tag{16}$$

where δ_{ij} is the Kronecker delta function.

The equation of motion of the elastic material of density ρ is given by Newton's second law:

$$\rho\frac{\partial^2 u_i}{\partial t^2} = \frac{\partial\sigma_{ij}}{\partial x_j}. \tag{17}$$

For the force per unit volume to be finite everywhere in the material, the stress tensor $\boldsymbol{\sigma}$ must be continuous everywhere. In the simple case of an isotropic linear elastic solid, using Eqs. (16) and (17) the dynamical equation simplifies to

$$\rho\frac{\partial^2 u_i}{\partial t^2} = \nabla\cdot(\mu\nabla u_i) + \nabla\cdot\left(\mu\frac{\partial\mathbf{u}}{\partial x_i}\right) + \frac{\partial}{\partial x_i}(\lambda\nabla\cdot\mathbf{u}). \tag{18}$$

Here the elastic Lamé coefficients appear in the differential operators, and these locally defined parameters could vary with position, as in our case of elastic composites. Equation (18) reveals that, while the elastic parameters and the strain may be discontinuous across material boundaries, the product stress tensor is continuous and differentiable everywhere for a finite force to act on each infinitesimal parcel. In the case of a homogeneous isotropic linear elastic solid, where the material parameters do not depend on the position, the Lamé coefficients could be factored out of the spatial derivatives to yield the conventional elastic equation [8,29].

C. Resonant oscillator unit cell

We consider a phononic crystal consisting of circular steel rods, arranged periodically in a square lattice of lattice constant $a = 1$ cm. Each circular steel rod is coupled to a stiff circular cellulose shell via open-cell foam. The background is the same type of open-cell foam. The steel core, cellulose shell, and interstitial foam fill $\phi_c = 20\%$, $\phi_s = 20\%$, and $\phi_f = 30\%$ by volume, respectively, so that the radius of the circular steel rod $R_1 = a\sqrt{\phi_c/\pi} \approx 0.2523$ cm, the inner radius of the circular cellulose shell $R_2 = a\sqrt{(\phi_c+\phi_f)/\pi} \approx 0.3989$ cm and the outer radius $R_3 = a\sqrt{(\phi_c+\phi_f+\phi_s)/\pi} \approx 0.4720$ cm. The material parameters of steel, cellulose, and foam are listed in Table I. The unit cell is depicted in Fig. 3.

D. Plane wave expansion and convergence of products

In the original work by Kushwaha [7,8] and in subsequent literature [18], the dynamical equation of an isotropic linear elastic solid is commonly expressed in terms of the density ρ and the longitudinal c_l and transverse c_t speeds of sound:

$$\rho\frac{\partial^2 u_i}{\partial t^2} = \nabla\cdot\left(\rho c_t^2\nabla u_i\right) + \nabla\cdot\left(\rho c_t^2\frac{\partial\mathbf{u}}{\partial x_i}\right) + \frac{\partial}{\partial x_i}\left[\left(\rho c_l^2 - 2\rho c_t^2\right)\nabla\cdot\mathbf{u}\right]. \tag{19}$$

The longitudinal and transverse speeds of sound are related to the Lamé parameters through $\lambda = \rho c_l^2 - 2\rho c_t^2$ and $\mu = \rho c_t^2$.

In photonics, the dielectric constant and the normal component of the electric field contain a pair of complementary

TABLE I. Tabulated are the density ρ, Lamé parameters of compression λ, and shear deformation μ of the relevant elastic solids. Mechanical data of steel are taken from sample number 11 from the experimental collection of 20 samples of steel which show small variations of 0.5%, 1.8%, and 0.9% in ρ, λ, and μ respectively [12]. Cellulose corresponds to cellulose nitrate thermoplastics commonly used for ping-pong balls with excellent machinability [30]. Open-cell foam refers to Type A foam containing 0.4 mm pores with 60 pores per inch manufactured by Foamex International Inc. [31] The mechanical moduli show modest anisotropy ratio of 1.0:1.1:1.4. This anisotropy is ignored as the foam is approximated by an isotropic solid.

Material	ρ (kg m^{-3})	λ (Pa)	μ (Pa)
Steel [12]	7940	1.075×10^{11}	7.815×10^{10}
Cellulose [30]	1350	1.21×10^{9}	5.19×10^{8}
Open-cell foam [31]	30	2.31×10^{4}	1.538×10^{4}

jump discontinuities, while the product electric displacement is continuous across material boundaries. Direct application of Fourier series in terms of electric field and dielectric constant results in poor numerical convergence, whereas numerical convergence is enhanced substantially by exploiting the continuity of the electric displacement [20,21,32]. In the case of elasticity, from the constitutive relation (15), the strain tensor $\boldsymbol{\epsilon}$ and the stiffness tensor $\mathbf{C}$ contain a pair of complementary jump discontinuities. The product stress tensor $\boldsymbol{\sigma}$ is continuous across material boundary. Rapid numerical is achieved, when the plane wave expansion scheme takes advantage of the continuity of the stress tensor. Instead of the dynamical equation (19) in terms of the speeds of sound, we start from the dynamical equation (18) involving the Lamé parameters. The Lamé parameters allow us to directly relate the strain and the stress tensors and the continuity of the stress tensor enables rapid numerical convergence. Algebraic details of the convergent procedures, relevant to our specific two-dimensional structure, are provided in Appendix A. In the remainder of this section, the acoustic Bloch waves and the decoupling of the out-of-plane mode from the in-plane modes are discussed.

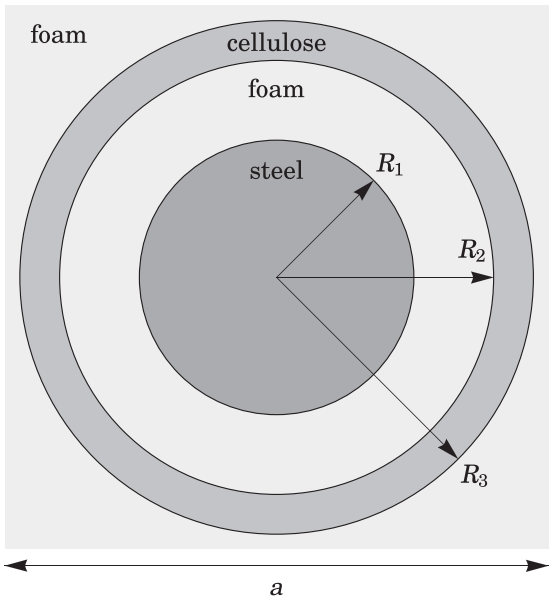

FIG. 3. A unit cell of a dense steel rod of radius $R_1 \approx 0.2523$ cm surrounded by a concentric circular cellulose shell of inner radius $R_2 \approx 0.3989$ cm and outer radius $R_3 \approx 0.4720$ cm with the interstitial spaces filled with open-cell foam in a square lattice of lattice constant $a = 1$ cm. The relevant material parameters are listed in Table I.

By discrete translational symmetry, the displacement vector field $\mathbf{u}$ satisfies the Bloch theorem, which states that the eigenfunction assumes the form of a plane wave modulated by a periodic function:

$$\mathbf{u}(\mathbf{r}, t) = \exp(i\mathbf{K}\cdot\mathbf{r} - i\omega_{\mathbf{K}}t)\sum_{\mathbf{G}}\mathbf{u}_{\mathbf{K}}(\mathbf{G})\exp(i\mathbf{G}\cdot\mathbf{r}). \quad (20)$$

Here $\mathbf{K}$ denotes the Bloch wave vector, $\mathbf{G}$ denotes a reciprocal lattice vector, $\mathbf{u}_{\mathbf{K}}(\mathbf{G})$ denotes the Fourier coefficient of the underlying periodic function, and $\omega_{\mathbf{K}}$ denotes the angular frequency. We refer to a combination of eigenvalue and eigenvector $(\omega_{\mathbf{K}}, \mathbf{u}_{\mathbf{K}}(\mathbf{G}))$ as an eigensolution.

We decompose the displacement field: $\mathbf{u} = u_x\hat{\mathbf{x}} + u_y\hat{\mathbf{y}} + u_z\hat{\mathbf{z}}$. The z-axis is aligned with the axis of rotational symmetry of the cylindrical steel core. The structure is translationally invariant in the z-direction, so that spatial derivatives with respect to z are null ($\partial/\partial z = 0$). The z-component of the displacement field describes transverse out-of-plane oscillation, while the x- and y-components describe in-plane motion. From Eq. (18), the dynamical equation of the out-of-plane displacement u_z reads

$$\frac{\partial}{\partial x}\left(\mu\frac{\partial u_z}{\partial x}\right) + \frac{\partial}{\partial y}\left(\mu\frac{\partial u_z}{\partial y}\right) + \rho\omega^2 u_z = 0. \quad (21)$$

When the Lamé parameter and the z-component of the displacement field are decomposed into Fourier series, an algebraic eigenvalue equation (A8) is obtained. The out-of-plane eigenvalues $\omega_{\mathbf{K}}$ are called the out-of-plane bands when plotted as a function of the Bloch wave vector $\mathbf{K}$.

While the in-plane displacement is decoupled from the out-of-plane displacement in Eq. (18), the x-component u_x and the y-component u_y are intricately coupled:

$$\frac{\partial}{\partial x}\left[(\lambda+2\mu)\frac{\partial u_x}{\partial x} + \lambda\frac{\partial u_y}{\partial y}\right] + \frac{\partial}{\partial y}\left[\mu\frac{\partial u_x}{\partial y} + \mu\frac{\partial u_y}{\partial x}\right] + \rho\omega^2 u_x = 0, \quad (22)$$

$$\frac{\partial}{\partial x}\left[\mu\frac{\partial u_x}{\partial y} + \mu\frac{\partial u_y}{\partial x}\right] + \frac{\partial}{\partial y}\left[\lambda\frac{\partial u_x}{\partial x} + (\lambda+2\mu)\frac{\partial u_y}{\partial y}\right] + \rho\omega^2 u_y = 0. \quad (23)$$

When the Lamé parameters and the displacement field are decomposed into Fourier series, an algebraic eigenvalue equation (A9) is obtained. These eigenvalue $\omega_{\mathbf{K}}$ describe the in-plane bands.

III. ANALYTICAL RIGID CORE-SHELL APPROXIMATION

Our resonant unit is composed of a dense cylindrical steel core, encapsulated by a stiff concentric cellulose shell, embedded in soft open-cell foam. The stiff steel core and the

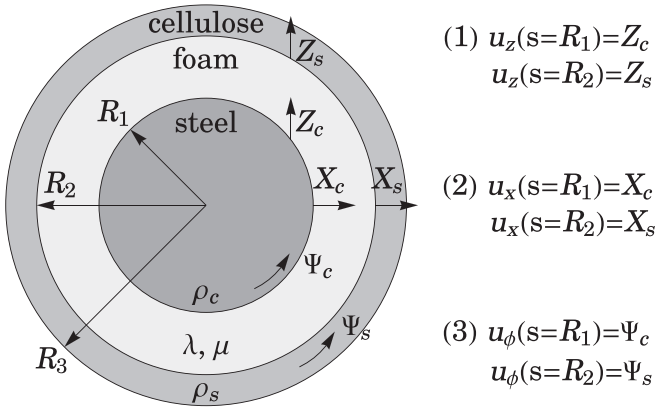

FIG. 4. A resonant unit is composed of a dense steel rod of radius $R_1 \approx 0.2523$ cm surrounded by a concentric stiff circular cellulose shell of inner radius $R_2 \approx 0.3989$ cm and outer radius $R_3 \approx 0.4720$ cm. The interstitial space is filled by elastic open-cell foam. The rigid cellulose shell and the steel core are disturbed from equilibrium with out-of-plane displacements Z_s and Z_c, in-plane translations X_s and X_c, and in-plane rotations Φ_s and Φ_c, respectively. The relevant material parameters are listed in Table I.

cellulose shell are approximated as rigid bodies. The interstitial foam is approximated as isotropic elastic material, governed by linear elastostatics. These approximations are collectively referred to as the rigid core-shell approximation (RCSA). The resonant modes are categorized into three types: (1) out-of-plane modes involving the relative translational motion of the rigid bodies in the axial direction, (2) in-plane translational modes involving their in-plane relative translations, and (3) in-plane rotational modes involving their in-plane relative rotations. These three modes are schematically depicted in Fig. 4.

By RCSA, we analytically derive closed-form, algebraic expressions for the frequency-dependent, effective mass densities for the out-of-plane and the in-plane motions. Analogies with the one-dimensional mass-in-a-box model are presented. Uniqueness of the solutions to the elastostatic boundary value problems, described in the subsequent subsections, are guaranteed by the finiteness of the total strain energy in the bounded region [33]. It suffices, therefore, to find one elastostatic equilibrium solution.

A. Out-of-plane resonance

In a two-dimensional phononic crystal with translation invariance in the axial direction, the out-of-plane oscillation is decoupled from the in-plane motion. The out-of-plane motion in each unit cell exhibits a local resonance. The cellulose shell and the steel core are elastically stiffer than the open-cell foam. The stiff shell and core are effectively approximated as rigid bodies, while the interstitial foam acts like an elastic spring. When the size of the resonant units is much smaller than the elastic wavelength, wave phenomena within each resonant unit can be neglected using an elastostatic approximation. Under this RCSA, we demonstrate how the out-of-plane motion is analytically mapped to the one-dimensional mass-in-a-box model.

We denote the out-of-plane displacement of the rigid cellulose shell by Z_s, and that of the rigid steel core by Z_c. Physically, when the steel core is displaced relative to the cellulose shell, elastic deformation of the open-cell foam provides a restoring force. We calculate this restoring force using two-dimensional, linear elasticity.

In the absence of external body force, the out-of-plane static displacement of the foam satisfies the Laplace equation. By rotational symmetry, the general solution to the out-of-plane displacement in cylindrical coordinates is

$$u_z(\mathbf{r}) = A_0 + B_0 \ln s + \sum_{n=1}^{\infty} \left(A_n s^n + \frac{B_n}{s^n}\right)[C_n \cos(n\phi) + D_n \sin(n\phi)], \tag{24}$$

where s and ϕ are radial and angular coordinates within the foam, and the constants A_n, B_n, C_n, and D_n are determined by the boundary conditions:

$$u_z(s = R_1) = Z_c, \tag{25a}$$

$$u_z(s = R_2) = Z_s. \tag{25b}$$

Straightforward substitution and orthogonality of the angular functions imply that only the $n = 0$ term survives:

$$A_0 = \frac{Z_c \ln R_2 - Z_s \ln R_1}{\ln R_2/R_1}, \tag{26a}$$

$$B_0 = \frac{Z_s - Z_c}{\ln R_2/R_1}, \tag{26b}$$

and $A_n = B_n = 0$ for all $n \geqslant 1$.

Essentially, RCSA allows us to drop the $n \neq 0$ terms that involve elastic deformation within the core and the shell. While the out-of-plane displacement field satisfies the Laplace equation, we show below in Sec. III B that the in-plane displacement field is governed by a set of coupled second-order differential equations. In this case, a solution different from Eq. (24) is required. For the out-of-plane displacement, we use the RCSA to write

$$\mathbf{u}(\mathbf{r}) = a(s)\hat{\mathbf{z}}, \tag{27}$$

where $a(s)$ is twice differentiable function of radial distance s, satisfying the following boundary conditions:

$$a(s = R_1) = Z_c, \tag{28a}$$

$$a(s = R_2) = Z_s. \tag{28b}$$

The only nonvanishing components of the symmetric strain tensor $\boldsymbol{\epsilon}$ are ϵ_{zs} and ϵ_{sz}:

$$\epsilon_{zs} = \epsilon_{sz} = \frac{1}{2}\left(\frac{\partial u_z}{\partial s} + \frac{\partial u_s}{\partial z}\right) = \frac{1}{2}\frac{da}{ds}. \tag{29}$$

Using the generalized Hooke's law for linear isotropic solids, expressed in Eq. (16), we conclude that the only nonvanishing components of the symmetric stress tensor $\boldsymbol{\sigma}$ are σ_{zs} and σ_{sz}:

$$\sigma_{zs} = \sigma_{sz} = 2\mu\epsilon_{sz} = \mu\frac{da}{ds}. \tag{30}$$

TABLE II. The equations of motion of the cellulose shell and the steel core (36) and (37) assume the same form as those in the mass-in-a-box model in (1) and (2). The correspondence of each physical parameter is tabulated below.

Mass-in-a-box model	Symbol	Resonant unit	Symbol
Mass of rigid box	m_1	Mass per unit length of cellulose shell	m_s
Mass of inner mass	m_2	Mass per unit length of steel core	m_c
Displacement of box	x_1	Out-of-plane displacement of cellulose shell	Z_s
Displacement of inner mass	x_2	Out-of-plane displacement of steel core	Z_c
Elastic spring constant	k	Elastic restoration of open-cell foam	k_z
Spring dissipation	c	Inelastic dissipation of open-cell foam	0

In the absence of an external body force, the stress tensor is divergence-free, $\partial\sigma_{ij}/\partial x_i = 0$, so that

$$\frac{1}{s}\frac{\partial}{\partial s}(s\sigma_{sz}) = \frac{1}{s}\frac{d}{ds}\left(s\mu\frac{da}{ds}\right) = 0. \tag{31}$$

We identify the preceding Eq. (31) as the Laplace equation, in cylindrical coordinates, within the foam region, for the rotationally symmetric function $a(s)$. Solving the Laplace equation and imposing the boundary conditions (28a) and (28b), we obtain

$$a(s) = A_0 + B_0 \ln s, \tag{32}$$

$$\sigma_{zs} = \sigma_{sz} = \frac{\mu B_0}{s}. \tag{33}$$

Next, the force per unit length acting on the steel core, $\mathbf{f}_{\mathrm{c},z}$, and that on the cellulose shell, $\mathbf{f}_{\mathrm{s},z}$, are determined from the stress tensor:

$$\mathbf{f}_{\mathrm{c},z} = \oint_{\{s=R_1\}} \boldsymbol{\sigma}\cdot\hat{\mathbf{n}}\, dl = 2\pi\mu B_0\hat{\mathbf{z}}, \tag{34}$$

$$\mathbf{f}_{\mathrm{s},z} = \oint_{\{s=R_2\}} \boldsymbol{\sigma}\cdot\hat{\mathbf{n}}\, dl = -2\pi\mu B_0\hat{\mathbf{z}}, \tag{35}$$

where $\hat{\mathbf{n}}$ is the inward normal unit vector on the boundary of the foam. Note that internal forces cancel $\mathbf{f}_{\mathrm{c},z} + \mathbf{f}_{\mathrm{s},z} = \mathbf{0}$, in agreement with Newton's third law.

The rigid body equations of motion of the cellulose shell and the iron core are expressed in Newton's second law:

$$m_\mathrm{s}\ddot{Z}_\mathrm{s} = f_z(\omega) + k_z(Z_\mathrm{c} - Z_\mathrm{s}), \tag{36}$$

$$m_\mathrm{c}\ddot{Z}_\mathrm{c} = k_z(Z_\mathrm{s} - Z_\mathrm{c}), \tag{37}$$

where $m_\mathrm{s} = \pi\rho_c(R_3^2 - R_2^2)$ is the mass of the cellulose shell per unit length, $m_\mathrm{c} = \pi\rho_s R_1^2$ is the mass of the steel core per unit length, $k_z = 2\pi\mu/(\ln R_2/R_1)$ denotes the spring constant per unit length, and $f_z(\omega)$ is the z-component of a harmonic force, acting on the cellulose shell, by the background foam, due to the relative motion between adjacent resonant units in the periodic structure.

In the one-dimensional mass-in-a-box model analogy, the cellulose shell is identified with the rigid box subject to an external force provided by the background open-cell foam. The steel core acts as the inner mass. The interstitial open-cell foam acts as the elastic spring. The equations of motion of the cellulose shell in (36) and the steel core in (37) assume the same form as those of the box in (1) and the inner mass in (2). The correspondence of each physical parameter is summarized in Table II.

Analogous to Eq. (11), the out-of-plane motion of the resonant oscillator can be described by an effective frequency-dependent density of the form

$$\rho_z^{(\mathrm{e})}(f) = \rho_\mathrm{s}\left(1 + \frac{f_{*,z}^2 - f_{0,z}^2}{f_{0,z}^2 - f^2}\right). \tag{38}$$

Here ρ_s is the mass of the cellulose shell divided by the volume occupied by the resonant unit:

$$\rho_\mathrm{s} = \frac{\pi\rho_c(R_3^2 - R_2^2)}{(\phi_\mathrm{c} + \phi_\mathrm{f} + \phi_\mathrm{s})a^2} \approx 385.7\ \mathrm{kg\ m^{-3}}, \tag{39}$$

$f_{0,z}$ (analogous to $\omega_0 = \sqrt{k/m_2}$) is the resonant frequency of the oscillator at which the effective mass diverges:

$$f_{0,z} = \frac{1}{2\pi}\sqrt{\frac{k_z}{m_\mathrm{c}}} \approx 183.4\ \mathrm{Hz}, \tag{40}$$

and $f_{*,z}$ [analogous to $\omega_* = \sqrt{k/m_\mathrm{r}}$ in Eq. (10)] is the frequency at which the effective mass density vanishes [$\rho_z^{(\mathrm{e})}(f = f_{*,z}) = 0$]:

$$f_{*,z} = \frac{1}{2\pi}\left[k_z\left(\frac{1}{m_\mathrm{c}} + \frac{1}{m_\mathrm{s}}\right)\right]^{1/2} \approx 481.2\ \mathrm{Hz}. \tag{41}$$

Using this effective mass model, we anticipate a phononic band gap for the out-of-plane modes over the frequency range $183.4\ \mathrm{Hz} < f < 481.2\ \mathrm{Hz}$, because wave propagation is prohibited in the negative effective density region where $f_{0,z} < f < f_{*,z}$.

B. In-plane translational resonance

We now consider the in-plane relative translation between the rigid cellulose shell and the rigid steel core. Suppose the cellulose shell and the steel core displace in the positive x-direction by X_s and X_c, respectively. Elastic deformation of the open-cell foam provides restoring forces, which we describe using basic two-dimensional linear elasticity.

In the RCSA, the displacement profile of the open-cell foam ($R_1 < s < R_2$) can be expressed as

$$\mathbf{u}(\mathbf{r}) = c_s(s)\cos\phi\ \hat{\mathbf{s}} + c_\phi(s)\sin\phi\ \hat{\boldsymbol{\phi}}, \tag{42}$$

where $c_r(s)$ and $c_\phi(s)$ are twice differentiable functions of radial distance, s. From $\mathbf{u}(s = R_{1/2}) = X_{\mathrm{c/s}}\hat{\mathbf{x}} = X_{\mathrm{c/s}}\cos\phi\ \hat{\mathbf{s}} - X_{\mathrm{c/s}}\sin\phi\ \hat{\boldsymbol{\phi}}$, it follows that the functions $c_s(s)$ and $c_\phi(s)$ satisfy

TABLE III. The equations of motion of the cellulose shell and the steel core (44) and (45) assume the same form as those in the mass-in-a-box model in Eqs. (1) and (2). The correspondence of each physical parameter is tabulated below.

Mass-in-a-box model	Symbol	Resonant unit	Symbol
Mass of rigid box	m_1	Mass per unit length of cellulose shell	m_s
Mass of inner mass	m_2	Mass per unit length of steel core	m_c
Displacement of box	x_1	In-plane displacement of cellulose shell	X_s
Displacement of inner mass	x_2	In-plane displacement of steel core	X_c
Elastic spring constant	k	Elastic restoration of open-cell foam	k_x
Spring dissipation	c	Inelastic dissipation of open-cell foam	0

the following boundary conditions:

$$c_s(s = R_1) = X_c, \tag{43a}$$

$$c_s(s = R_2) = X_s, \tag{43b}$$

$$c_\phi(s = R_1) = -X_c, \tag{43c}$$

$$c_\phi(s = R_2) = -X_s. \tag{43d}$$

The elasticity analysis of in-plane translational modes in the annular region of interstitial foam parallels that of the out-of-plane modes in Sec. III A. We summarize the key physical concepts here with the algebraic details provided in Appendix B. The nonvanishing components of the strain tensor are determined from the displacement profile in (42). Hooke's law in linear elasticity relates the strain tensor and the divergenceless stress tensor in the absence of an external body force. The resultant boundary value problem in $\{c_s, c_\phi\}$ is solved in closed form, and the forces acting on the cellulose shell and the steel core are determined by integration around the boundaries of the annular foam region.

Using the derivations provided in Appendix B, the equations of motion of the cellulose shell and the iron core are given by

$$m_s\ddot{X}_s = f_x(\omega) + k_x(X_c - X_s), \tag{44}$$

$$m_c\ddot{X}_c = -k_x(X_c - X_s). \tag{45}$$

Here k_x is the elastic spring constant per unit length given by Eqs. (B8) and (B9) in Appendix B:

$$k_x = 4\pi\mu(\lambda + 2\mu)(\lambda + 3\mu)\left(R_1^2 + R_2^2\right)\left[(\lambda + 3\mu)^2 \times \left(R_1^2 + R_2^2\right)\ln R_2/R_1 - (\lambda + \mu)^2\left(R_2^2 - R_1^2\right)\right]^{-1}. \tag{46}$$

m_s and m_c denote the mass per unit length of the cellulose shell and the steel core, respectively. $f_x(\omega)$ is the x-component of a harmonic force acting on the cellulose shell by the background foam due to the relative motion between neighboring resonant units in the phononic crystal.

To complete the analogy with the one-dimensional mass-in-a-box model, we identify the cellulose shell with a rigid box harmonically coupled to the background open-cell foam, the steel core with the inner mass, and the interstitial open-cell foam with the elastic spring. The correspondence of each physical parameter is summarized in Table III.

Consequently, the in-plane translational resonance can be described by a frequency-dependent effective mass density:

$$\rho_t^{(e)}(f) = \rho_s\left(1 + \frac{f_{*,t}^2 - f_{0,t}^2}{f_{0,t}^2 - f^2}\right). \tag{47}$$

Here $\rho_s \approx 385.8$ kg m^{-3} is mass of the cellulose shell divided by the volume occupied by the resonant unit in Eq. (39). $f_{0,t}$ (analogous to $\omega_0 = \sqrt{k/m_2}$) is the resonant frequency of the oscillator at which the effective mass diverges:

$$f_{0,t} = \frac{1}{2\pi}\sqrt{\frac{k_x}{m_c}} \approx 271.3 \text{ Hz}. \tag{48}$$

$f_{*,t}$ (analogous to $\omega_* = \sqrt{k/m_r}$) is the frequency at which the effective in-plane mass vanishes:

$$f_{*,t} = \frac{1}{2\pi}\left[k_x\left(\frac{1}{m_c} + \frac{1}{m_s}\right)\right]^{1/2} \approx 711.7 \text{ Hz}. \tag{49}$$

Over the frequency range $f_{0,t} < f < f_{*,t}$ of negative effective mass, wave propagation involving the in-plane translation of the resonant unit is suppressed.

C. In-plane rotational resonance

We now derive another frequency-dependent effective density describing the relative rotation between the steel core and the cellulose shell, and the elastic deformation of the open-cell foam providing restoring torques. We determine such restoring torques using two-dimensional, linear elasticity.

Suppose the rigid cellulose shell rotates by an angle Ψ_s counterclockwise, and the rigid steel core rotates by Ψ_c. By RCSA, the displacement depends only on the radial distance s:

$$\mathbf{u}(\mathbf{r}) = b(s)\hat{\boldsymbol{\phi}}, \tag{50}$$

where $b(s)$ is twice differentiable function of radial distance, s, satisfying the boundary conditions:

$$b(s = R_1) = R_1\Psi_c, \tag{51a}$$

$$b(s = R_2) = R_2\Psi_s. \tag{51b}$$

The elasticity analysis of in-plane rotational modes in the annular region of interstitial foam is provided in Appendix C. Under rotational symmetry, the strain and stress tensors simplify. The nonvanishing components are determined from the displacement profile (50). The solution $b(s)$ is expressible in closed form, and the torques acting on the cellulose shell and the steel core are determined by integration around the boundaries of the annular foam region.

The moment of inertia per unit length of the cellulose shell, I_s, and that of the steel core, I_c, are given

TABLE IV. The equations of motion of the cellulose shell and the steel core (55) and (56) assume the same form as those in the mass-in-a-box model in (1) and (2). The correspondence of each physical parameter is tabulated below.

Mass-in-a-box model	Symbol	Resonant unit	Symbol
Mass of rigid box	m_1	Rotational inertia of cellulose shell	I_s
Mass of inner mass	m_2	Rotational inertia of steel core	I_c
Displacement of box	x_1	Angle of rotation of cellulose shell	Ψ_s
Displacement of inner mass	x_2	Angle of rotation of steel core	Ψ_c
Elastic spring constant	k	Elastic restoration of open-cell foam	k_ϕ
Spring dissipation	c	Inelastic dissipation of open-cell foam	0

by

$$I_s = \int_{R_2}^{R_3} \rho_s s^2 2\pi s\, ds = \frac{\pi}{2}\rho_s\left(R_3^4 - R_2^4\right), \tag{52}$$

$$I_c = \int_{0}^{R_1} \rho_c s^2 2\pi s\, ds = \frac{\pi}{2}\rho_s R_1^4. \tag{53}$$

The elasticity analysis in Appendix C yields an elastic restoring torque per angular displacement [see Eqs. (C7) and (C8)]:

$$k_\phi = \frac{4\pi\mu R_1^2 R_2^2}{R_2^2 - R_1^2}. \tag{54}$$

The equations of rotational motion of the cellulose shell and the iron core take the form

$$I_s\ddot{\Psi}_s = \tau(\omega) + k_\phi(\Psi_c - \Psi_s), \tag{55}$$

$$I_c\ddot{\Psi}_c = +k_\phi(\Psi_s - \Psi_c). \tag{56}$$

Here $\tau(\omega)$ is the harmonic torque acting on the cellulose shell by the background foam due to the relative motion between adjacent resonant units in the periodic structure.

In the one-dimensional mass-in-a-box analogy, the cellulose shell is identified with the rigid box subject to harmonic force by coupling with the background open-cell foam. The steel core is the inner mass. The interstitial open-cell foam acts as the elastic spring. The correspondence of each physical parameter is summarized in Table IV. The rotational motion of the resonant oscillator can be recaptured by a frequency-dependent effective density of the form

$$\rho_r^{(e)}(f) = \rho_r\left(1 + \frac{f_{*,r}^2 - f_{0,r}^2}{f_{0,r}^2 - f^2}\right). \tag{57}$$

Here ρ_r is the density of an effective uniform cylinder of radius R_3 that yields the same moment of inertia as the actual cellulose shell:

$$\rho_r = \frac{\rho_s\left(R_3^4 - R_2^4\right)}{R_3^4} = 661.2\ \text{kg m}^{-3}. \tag{58}$$

$f_{0,r}$ (analogous to $\omega_0 = \sqrt{k/m_2}$) is the resonant frequency of the oscillator at which the effective moment of inertia diverges:

$$f_{0,r} = \frac{1}{2\pi}\sqrt{\frac{k_\phi}{I_c}} \approx 320.6\ \text{Hz}, \tag{59}$$

and $f_{*,r}$ (analogous to $\omega_* = \sqrt{k/m_r}$) is the frequency at which the effective rotational inertia vanishes:

$$f_{*,r} = \frac{1}{2\pi}\left[k_\phi\left(\frac{1}{I_c} + \frac{1}{I_s}\right)\right]^{1/2} \approx 451.1\ \text{Hz}. \tag{60}$$

In the frequency range of negative effective density ($f_{0,r} < f < f_{*,r}$), wave propagation involving rotational motion of the resonant unit is inhibited.

IV. NUMERICAL COMPARISON OF EFFECTIVE MASS MODEL WITH EXACT BAND STRUCTURE

We now calculate and compare the acoustic band structures for the original, locally resonant, phononic crystals and the frequency-dependent, effective mass, phononic crystal. The former is calculated using a Finite Element Method (FEM). The latter is calculated using a plane wave expansion combined with the Cutting Surface Method (CSM) [17] to treat the frequency-dependent mass. We verify that the out-of-plane band structure exhibits a band gap at negative effective density over the frequency range $f_{0,z} < f < f_{*,z}$, which agrees with the exact FEM results within 2% accuracy at all the wave vectors considered. For in-plane band structure, the agreement between the true resonant medium and the frequency-dependent, effective mass medium is limited to points specific in the phononic Brillouin zone.

A. Cutting Surface Method

The Cutting Surface Method (CSM) was introduced earlier [17] to determine the optical band structure of photonic crystals with frequency-dependent dielectric constant $\epsilon(\omega)$. In this method, a generalized electromagnetic dispersion relation $\omega(\mathbf{K}, \epsilon_p)$ is first evaluated parametrically as a function of a hypothetical dielectric constant ϵ_p, wherever the actual dielectric constant is frequency-dependent, and the resultant dispersion surfaces are cut by the requirement of $\epsilon_p = \epsilon(\omega)$ to yield the true band structure along the cutting surface [17]. For our locally resonant phononic crystal, an effective, frequency-dependent density $\rho_z^{(e)}(f)$ is used to represent the resonant unit. A generalized acoustic dispersion relation, $f(\mathbf{K}, \rho_p)$, is calculated parametrically as a function of a hypothetical density ρ_p. Then, the required dispersion relation is determined by cutting the generalized dispersion relation by imposing the condition $\rho_p = \rho_z^{(e)}(f)$. The effective medium representation is depicted in Fig. 5.

The CSM relies heavily on the continuities of the generalized dispersion relation and the frequency dependence of

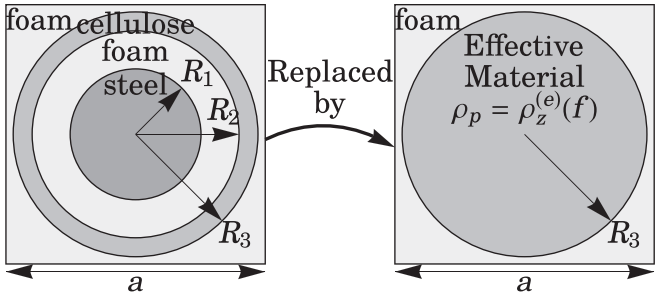

FIG. 5. The left panel shows a unit cell of the resonant composite structure consisting of a cylindrical circular steel rod of radius $R_1 \approx 0.2523$ cm, encapsulated by a coaxial circular cellulose shell of inner radius $R_2 \approx 0.3989$ cm and outer radius $R_3 \approx 0.4720$ cm with the interstitial region filled by open cell foam in a square lattice of lattice constant $a = 1$ cm. In the CSM, the resonant unit is replaced by an effective material with frequency-dependent density $\rho_z^{(e)}(f)$ in Eq. (38), while the open-cell foam background remains unchanged. The effective material assumes the frequency-independent Lamé parameters of cellulose. The relevant material parameters are listed in Table I.

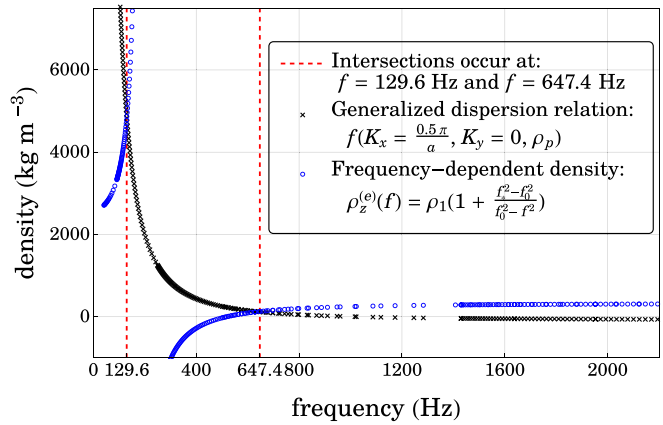

FIG. 6. At $(K_x, K_y) = (0.5\pi/a, 0)$, the generalized dispersion relation, $f(K_x = 0.5\pi/a, K_y = 0, \rho_p)$, represented by black crosses, and the frequency-dependent density, $\rho_z^{(e)}(f)$ in Eq. (38), represented by blue circles, intersect at $f \approx 129.6$ Hz and $f \approx 647.4$ Hz. Similarly, at other **K** points in the reciprocal space, there are two intersections, one below the resonant frequency $f < f_{0,z} \approx 183.4$ Hz and one above the zero-effective density frequency $f > f_{*,z} \approx 481.2$ Hz.

physical parameters in the neighborhood of the intersection points. In regions where the physical parameters depend sensitively on frequency, more sampling points in the parameter space are required to ensure accuracy and reliability of the numerical results.

Our effective medium consists of a phononic crystal of parallel, right, circular cylinders with uniform, frequency-dependent density occupying $\phi_c + \phi_f + \phi_s = 70\%$ by volume and open-cell foam filling the background. The harmonic interactions between resonant units are treated exactly, while the response within each resonant unit is captured by the frequency-dependent, effective density. A collection of band structures is determined by plane wave expansion, as the hypothetical uniform density of the cylinders is varied parametrically from $\rho_p = 0.5$ kg m^{-3} to $\rho_p = 20\,000$ kg m^{-3}. The Lamé parameters of the replacement material are chosen to be those of cellulose. The relevant material parameters are listed in Table I. A total of 298 band structures were calculated using 21 plane waves per direction. Details of plane wave convergence using an "inverse rule" for Fourier series multiplication of functions with complementary discontinuities are presented in Appendix A.

With the generalized acoustic dispersion, $f(\mathbf{K}, \rho_p)$, we impose the frequency-dependent density in Eq. (38) by intersection with the cutting surface $\rho_p = \rho_z^{(e)}(f)$. For illustration, the generalized dispersion relation at $\mathbf{K} = \pi/(2a)\hat{\mathbf{x}}$ and the frequency-dependent density, $\rho_z^{(e)}(f)$, are plotted in Fig. 6. At this **K**-point, the frequency-dependent density intersects the generalized dispersion relation at $f \approx 129.6$ Hz and again at $f \approx 647.4$ Hz. To enhance numerical accuracy, linear interpolation of the generalized acoustic dispersion, $f(\mathbf{K}, \rho_p)$, is used to determine the intersecting frequencies. The same numerical routine is repeated at all **K**-points in the reciprocal space to obtain the acoustic band structure of the effective medium phononic crystal. At all **K**-points, two intersections occur, one in the frequency range $0 \leqslant f < f_{0,z} \approx 183.4$ Hz and another in the range $f_{*,z} \approx 481.2$ Hz $< f$. This means that the first acoustic surface of the generalized dispersion relation splits into two disconnected bands, corresponding to the in-phase and out-of-phase oscillations of the core and the shell of the resonant unit. The resulting band structure of the effective medium phononic crystal is plotted in Fig. 7.

B. Finite Element Method

Commercial Finite Element Method (FEM) packages, COMSOL Multiphysics together with the Acoustic Module, provide an accurate and independent numerical calculation of

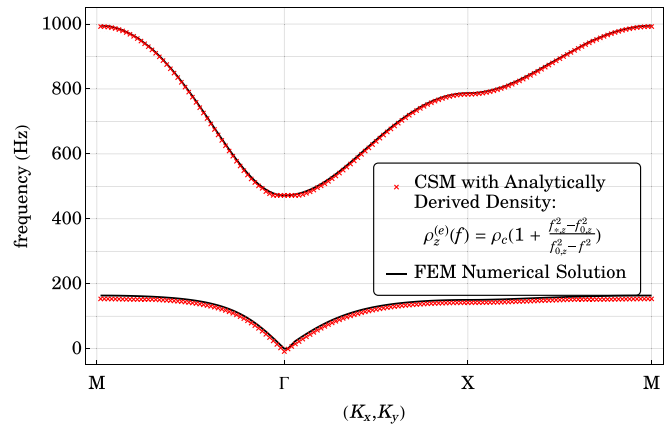

FIG. 7. First two out-of-plane acoustic bands of the steel-cellulose-foam phononic crystal are plotted in the first Brillouin zone along the path $M \to \Gamma \to X \to M$. The Cutting Surface Method (red crosses), together with plane wave expansion is used to calculate bands of a frequency-dependent, effective, mass phononic crystal. The finite element method (solid black line) is used to calculate bands of the actual phononic crystal. The maximum percentage error of the effective medium representation in the lower band is 1.2%, while that of the upper band is 1.9%.

the true resonant acoustic band structure. Each solid component of the phononic crystal is modeled by a lossless isotropic elastic material. Floquet periodic boundary conditions are imposed across the sides of a unit cell in the square lattice. The square unit cell is set to be 1 cm × 1 cm. The calculations are set to include time-harmonic out-of-plane modes in the two-dimensional model of solid mechanics. For numerical accuracy and stability, the maximum separation between neighboring mesh points is set to be at most one-tenth of the wavelength at the cutoff frequency of 2100 Hz. The edges of the unit cell are set to have identical mesh geometry. A fine mesh with 434 domain elements and 124 boundary elements is obtained, and the resultant eigenvalue problem is solved iteratively using MUltifrontal Massively Parallel sparse direction Solver (MUMPS) [34]. The first two out-of-plane bands of the true phononic crystal, obtained by FEM, are plotted in Fig. 7, together with the CSM results for the frequency-dependent, effective mass, phononic crystal.

C. Out-of-plane acoustic band structures

Figure 7 shows that the out-of-plane acoustic band structure obtained by CSM using the analytically derived frequency-dependent effective density agrees closely with the FEM results for the original phononic crystal. The maximum percentage deviation in frequency of the lower band is 1.2%, while that of the upper band is 1.9%.

There is an acoustic band gap from 163.7 Hz to 472.1 Hz. This is consistent with the rough prediction that wave propagation is prohibited at negative effective density over the frequency range, $f_{0,z} \approx 183.4\ \text{Hz} < f < f_{*,z} \approx 481.2\ \text{Hz}$. It is expected that the lower edge of the band gap lies slightly below the resonant frequency, because the first intersection occurs before the effective density diverges to infinity on resonance. On the other hand, the 1.9% error of the upper edge of the band gap may be attributed to the elastostatic approximation. In deriving the frequency-dependent effective density, we assumed that the wavelength of sound is long compared to the relevant dimensions of the resonant unit. In other words, wave phenomena in the interstitial open-cell foam is omitted. In reality, it takes time for a deformation to propagate from the outer cellulose shell to the inner steel core, leading to a phase lag between the motion of the two rigid bodies. At the upper edge of the band gap, 472.1 Hz, the wavelength in open-cell foam is $\lambda_f \approx 4.80$ cm, while the thickness of the foam layer within the rigid bodies is $R_2 - R_1 \approx 0.147$ cm. In this case, a relative error of about $(R_2 - R_1)/\lambda_f \approx 3.1\%$ can be anticipated.

Figures 8 and 9 show the normalized out-of-plane displacement in a unit cell at $(K_x, K_y) = (0.5\pi/a, 0)$ for the in-phase mode and the antiphase mode respectively. The accompanying density plots show that the displacement profiles are radially symmetric within the resonator $s < R_3$. In both cases, the out-of-plane displacement is constant over the ranges $s < R_1$ and $R_2 < s < R_3$, which underscore the validity of the RCSA. In the lower frequency mode at $f = 129.6\ \text{Hz} < f_{0,z}$, the RCSA predicts [see Eq. (3)] that the core and the shell oscillate in-phase with relative amplitude $Z_c/Z_s = f_{0,z}^2/(f_{0,z}^2 - f^2) \approx 2.00$. On the other hand, in the higher frequency mode at $f = 647.4\ \text{Hz} > f_{0,z}$, the RCSA predicts that the

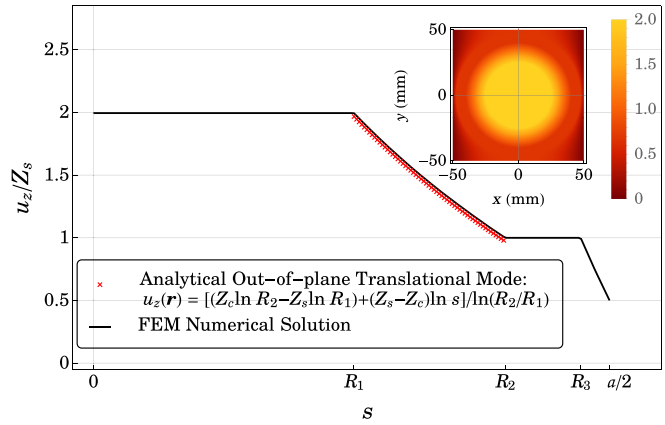

FIG. 8. At $(K_x, K_y) = (0.5\pi/a, 0)$, the normalized out-of-plane displacement of the in-phase mode at $f = 129.6$ Hz is plotted from $(x, y) = (0.0)$ to $(x, y) = (a/2, 0)$, for the finite element method (black line). A density plot of the displacement profile is shown at upper right corner. The constancy of the displacement in the regions $s < R_1$ and $R_2 < s < R_3$ correspond to the rigidity of the steel core and the cellulose shell respectively. The RCSA in Eq. (32) (red crosses) is plotted over the region of the interstitial foam $R_1 < s < R_2$, with the maximum error of $(0.0022)Z_s$.

core and the shell oscillate antiphase with relative amplitude $Z_c/Z_s = f_{0,z}^2/(f_{0,z}^2 - f^2) \approx -0.087$. The relative amplitudes agree with the constant displacement values of the steel core $s < R_1$ in the normalized displacement graphs. The displacement variations in the interstitial foam $R_1 < s < R_2$ are accurately recaptured by the RCSA in Eq. (32) (red crosses) within the errors of $(0.0022)Z_s$ for the in-phase mode, and $(0.0044)Z_s$ for the antiphase mode.

For comparison purposes, we also consider a frequency-independent, mean density representation of the resonant unit.

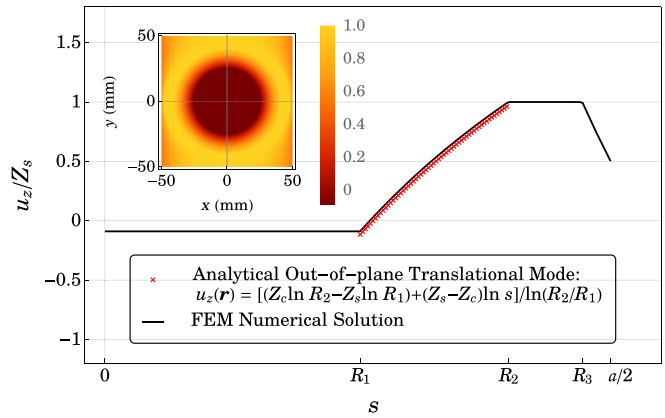

FIG. 9. At $(K_x, K_y) = (0.5\pi/a, 0)$, the normalized out-of-plane displacement of the antiphase mode at $f = 647.4$ Hz is plotted from $(x, y) = (0.0)$ to $(x, y) = (a/2, 0)$, for the finite element method (black line). A density plot of the displacement profile is shown at upper left corner. The constancy of the displacement in the regions $s < R_1$ and $R_2 < s < R_3$ correspond to the rigidity of the steel core and the cellulose shell, respectively. The RCSA in Eq. (32) (red crosses) is plotted over the region of the interstitial foam $R_1 < s < R_2$, with the maximum error of $(0.0044)Z_s$.

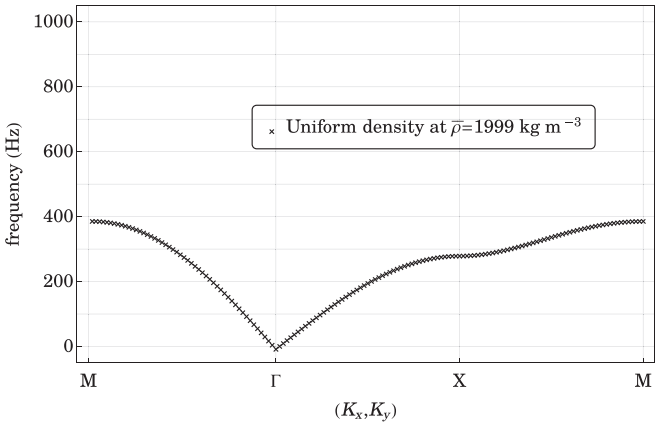

FIG. 10. Lowest out-of-plane acoustic band of the frequency-independent, mean-density representation of the locally resonant phononic crystal is plotted in the first Brillouin zone along the path $M \to \Gamma \to X \to M$. This consists of right circular cylinders of radius, R_3, of equivalent mean density $\bar{\rho} = \phi_c\rho_c + \phi_f\rho_f + \phi_s\rho_s \approx 1999\ \mathrm{kg\ m^{-3}}$, embedded in open-cell foam. There is only one out-of-plane acoustic band over the plotted frequency range. The over-simplified mean-density model fails to capture the resonant response of the true phononic crystal.

The simplest representation of the resonant unit is a uniform density material of equivalent mean density $\bar{\rho} = \phi_s\rho_s + \phi_c\rho_c + \phi_f\rho_f = 1999\ \mathrm{kg\ m^{-3}}$. We choose the Lamé parameters of the replacement material to match those of cellulose. Plotted in Fig. 10 is the associated acoustic band structure of a square lattice of rigid right cylinders of density $\bar{\rho} = 1999\ \mathrm{kg\ m^{-3}}$, occupying 70% by volume, embedded in open-cell foam. There is only one acoustic band over the plotted frequency range, while the frequency of the next out-of-plane band occurs around 3294 Hz. Clearly, the mean-density model fails to capture even the low-frequency resonance response of the actual phononic crystal.

In the frequency-dependent model, the lower band is pushed lower, but the upper band is pushed higher. This is consistent with the values of the frequency-dependent, effective density, which increases from $2653\ \mathrm{kg\ m^{-3}}$ at $f = 0$ Hz to infinity at $f = f_{0,z} \approx 183.4$ Hz. Since the frequency-dependent, effective density is consistently higher than the mean density $\bar{\rho} = 1999\ \mathrm{kg\ m^{-3}}$, the lower band is red-shifted. On the other hand, over the range $f > f_{*,z} \approx 481.2$ Hz, the frequency-dependent, effective density increases from 0 at $f = f_{*,z}$ to $\rho_c \approx 385.7\ \mathrm{kg\ m^{-3}}$ as f approaches infinity, which is consistently lower than the mean density, $\bar{\rho} = 1999\ \mathrm{kg\ m^{-3}}$. Consequently, the upper band is blue-shifted.

D. In-plane acoustic band structure

We now describe the challenges of extending the effective mass representation of the phononic crystal to the in-plane acoustic band structure of the steel-cellulose-foam resonant composite. The coupling between in-plane translation and rotation complicates the use of any simple, frequency-dependent, effective mass formula. A more elaborate representation is required to recapture all features of the true band structure.

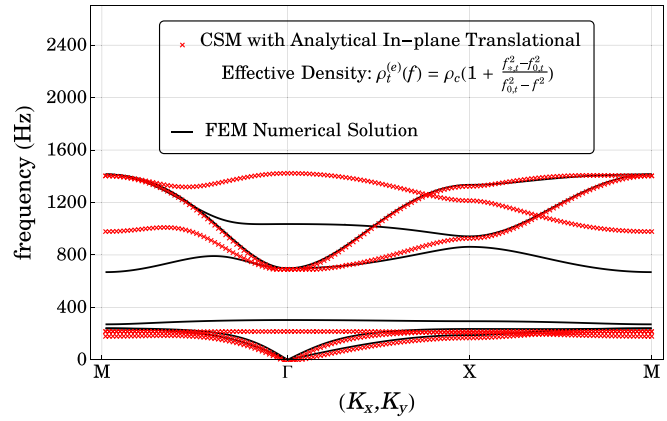

FIG. 11. First six in-plane acoustic bands of the periodic steel-cellulose-foam composite are plotted in the first Brillouin zone along the path $M \to \Gamma \to X \to M$, for the Cutting Surface Method (red crosses) using the frequency-dependent, effective density for in-plane translations in Eq. (47). The finite element method (solid black line) is used to calculate the bands of the actual phononic crystal.

For any single type of local resonance, the generalized in-plane acoustic band structure $f(\mathbf{K}, \rho_p)$ is determined parametrically as a function of the density ρ_p of a hypothetical uniform medium. The numerical setup for generating a parametric collection of band structures parallels that of the out-of-plane CSM calculations in the preceding section. As a first attempt to represent the in-plane internal translational and rotational resonances, the generalized in-plane acoustic band structure is separately cut by the frequency-dependent effective densities for in-plane translation $\rho_{\mathrm{t}}^{(\mathrm{e})}(f)$ in Eq. (47) and that for in-plane rotation $\rho_{\mathrm{r}}^{(\mathrm{e})}(f)$ in Eq. (57). The separate, resultant band structures are plotted in Figs. 11 and 12, and compared with FEM results for the original phononic crystal.

The in-plane acoustic band structures of the steel-cellulose-foam composite consists of six bands below 1500 Hz. The first three bands are separated from the next three bands by

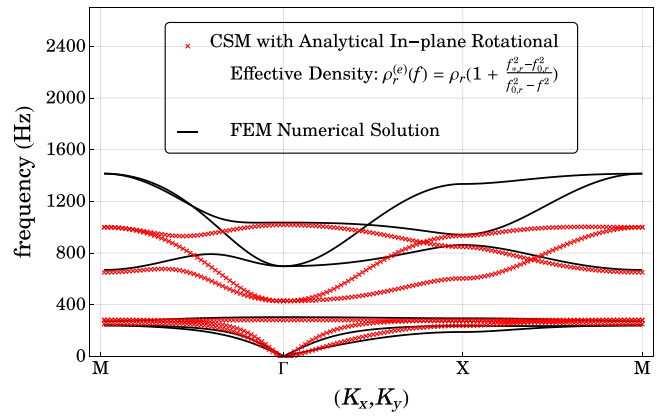

FIG. 12. First six in-plane acoustic bands of the periodic steel-cellulose-foam composite are plotted in the first Brillouin zone along the path $M \to \Gamma \to X \to M$, for the Cutting Surface Method (red crosses) using the frequency-dependent, effective density for in-plane rotations in Eq. (57). The finite element method (solid black line) is used to calculate the bands of the actual phononic crystal.

a gap over the frequency range 303.3 Hz $< f <$ 669.8 Hz. The first three bands are associated with in-phase relative rotation and translation between the rigid steel core and the cellulose shell in two orthogonal directions, while the next three bands arise from the corresponding antiphase relative motion.

Neither the effective density for in-plane translation nor that for in-plane rotation accounts for the true acoustic band structure at all **K**-points. However, some qualitative features of the actual in-plane bands are recaptured. First, there are six bands in all cases. The simple pole of the frequency-dependent effective density on resonance gives rise to two intersections with each of the three bands in the nonresonant generalized in-plane acoustic band structure, with one below the resonant frequency $f < f_{0,\mathrm{t/r}}$ and the other above the zero-density frequency $f > f_{0,\mathrm{t/r}}$. Moreover, the elasticity analysis for in-plane rotation predicts that in-plane rotational modes are inhibited over the frequency range $f_{0,\mathrm{r}} \approx 320.6$ Hz $< f < f_{*,\mathrm{r}} \approx 451.1$ Hz. This lies completely within the actual in-plane acoustic band gap 303.3 Hz $< f <$ 669.8 Hz. On the other hand, the effective medium representation for in-plane translation suggests the inhibition of in-plane translational modes over the frequency range $f_{0,\mathrm{t}} \approx 271.3$ Hz $< f < f_{*,\mathrm{t}} \approx 711.7$ Hz. Modes that are poorly represented by the effective density for in-plane translation are better described by in-plane rotation, and vice versa. At high symmetry points in the Brillouin zone, where the translational and rotational motion are decoupled, the resonant frequency is well represented by a single effective density.

These observations suggest that the translational and rotational motion are intricately coupled except at the high symmetry points. In band structure of the true phononic crystal, the path from $\Gamma(\mathbf{K} = \mathbf{0})$ to M ($\mathbf{K} = \pi/a\hat{\mathbf{x}} + \pi/a\hat{\mathbf{y}}$) leads from pure rotational mode at Γ to the pure translational mode at M. The in-plane coupling of the translational/rotational resonance in one unit cell to the rotational/translational resonance in a neighboring unit cell is not captured by the simplest effective medium representation of the phononic crystal. This is unlike the out-of-plane resonance in one unit cell that couples only to the same type of resonance in another unit cell. A more elaborate effective medium representation is needed to treat a resonant medium where cross-coupling occurs between different resonances at separate locations.

V. DISCUSSION AND CONCLUSIONS

In this paper, we have demonstrated by analytical and numerical means, the efficacy of the frequency-dependent, effective, mass density representation of a locally resonant acoustic material with a single type of resonance. For a periodic array of such local resonances, we obtained the exact modes of the phononic crystal by applying a Cutting Surface Method to calculate acoustic band structure. Our analysis also reveals the need for a fundamental generalization of the simple one-dimensional mass-in-a-box model of local resonances when the resonant unit contains multiple resonances that couple nontrivially to those in the neighboring resonant units.

Future directions include the extension of the analysis to three-dimensional resonant units, nonperiodic systems and dissipative materials. The elasticity analysis in this article applies to each individual resonant unit and does not rely on periodicity. While acoustic band structure derives from spatial periodicity, our elasticity calculation for each resonant unit applies to a medium with randomly placed resonant units. An important generalization of our analytical treatment is to spherical local resonators in a three-dimensional elastic medium. This involves a generalization of our methodology in Sec. III from cylindrical to spherical coordinates. It also requires generalizing our plane-wave expansion in Appendix A. However, this is likely to introduce a larger number of low-frequency resonances and their couplings between different unit cells. It is prudent to first solve the issues of multiple resonances and their nontrivial couplings in the simpler two-dimensional system.

By introducing the Rigid Core-Shell Approximation, we obtained a simple, analytical derivation of the frequency-dependent, effective densities for out-of-plane translational, in-plane translational, and in-plane rotational resonances. Our resonator, composed of a steel core, surrounded by foam, and encapsulated by a cellulose shell, also reveals that very low-frequency resonant modes can be realized with centimeter-sized resonant units. Moreover, an array of such units provides low-frequency flat bands in the acoustic band structure. This corresponds to high density of slow-sound modes and may be very effective in absorbing audible sound waves using a relatively thin sheet of resonant material with dissipation. Enhanced absorption effects of this type have been shown in photonic crystal thin films [35]. Recapturing these effects in acoustic materials, using realistic, frequency-dependent, effective mass models, is highly desirable. Given the real-world, locally resonant, acoustic materials may contain multiple nearby resonances, a generalization of the simple one-dimensional mass-in-a-box model is needed to properly capture all the relevant physics.

ACKNOWLEDGMENTS

This work was supported in part by the Natural Science and Engineering Research Council of Canada. K.L.S.Y. acknowledges receipt of Cray Fellowships in Physics.

APPENDIX A: CONVERGENCE OF ACOUSTIC PLANE WAVE EXPANSION

We describe the out-of-plane and in-plane eigenvalue equations of acoustic band structure, specific to our two-dimensional structures. Discrete translational symmetry allows expansion of material parameters into Fourier series:

$$\rho(\mathbf{r}) = \sum_{\mathbf{G}} \rho(\mathbf{G}) \exp(i\mathbf{G}\cdot\mathbf{r}), \tag{A1}$$

$$(1/C_{pqrs})(\mathbf{r}) = \sum_{\mathbf{G}} (1/C_{pqrs})(\mathbf{G}) \exp(i\mathbf{G}\cdot\mathbf{r}). \tag{A2}$$

Here $\mathbf{G}$ denotes reciprocal lattice vectors determined by the periodicity of the underlying lattice, C_{pqrs} denotes a nonzero element of the stiffness tensor $\mathbf{C}$, and $1/C_{pqrs}$ is the reciprocal

of that element. The Fourier coefficients are given by

$$\mathcal{M}(\mathbf{G}) = \frac{1}{A_c}\int_c d^2\mathbf{r}\mathcal{M}(\mathbf{r})\exp(-i\mathbf{G}\cdot\mathbf{r}). \tag{A3}$$

Here the integration is performed over the unit cell, and A_c is its area. $\mathcal{M}$ denotes a generic mechanical parameter, including the mass density, ρ, and the reciprocal of nonzero stiffness tensor components $1/\lambda$, $1/\mu$ and $1/(\lambda+2\mu)$. It is conventional to truncate the summation over the reciprocal lattice vectors: $-2\pi N/a \leqslant G_{x/y} \leqslant 2\pi N/a$, so that there are $(2N+1)$ plane waves per direction. Unless otherwise specified, the value of $N = 10$ is assumed in the plane wave expansion.

In the effective medium representation of the phononic crystal, each resonant unit (within the radius R_3) is replaced by a material of uniform, frequency-dependent density. The Lamé parameters of the replacement material are chosen to be those of cellulose in Table I. The filling fraction, $\nu = \pi R_3^2/a^2 = 0.7$, is the fractional volume occupied by the circular resonant unit in the square unit cell. In the effective medium in which all mechanical parameters are uniform when $s < R_3$, the Fourier components of each parameter take the form [8,18]

$$\mathcal{M}(\mathbf{G}) = \begin{cases} \mathcal{M}_a\nu + \mathcal{M}_b(1-\nu), & \text{for } \mathbf{G} = 0, \\ (\mathcal{M}_a - \mathcal{M}_b)2\nu J_1(GR_3)/GR_3, & \text{for } \mathbf{G} \neq 0. \end{cases} \tag{A4}$$

Here $\mathcal{M}_a$ is the value of the parameter when $s < R_3$, and $\mathcal{M}_b$ is its value in the background foam. J_1 is the Bessel function of the first kind of order 1. When the parameter $\mathcal{M}_a$ represents the mass density, it exhibits the prescribed frequency dependence, leading to a nonlinear eigenvalue problem, which is solved by CSM.

In the constitutive relation (15), the strain tensor $\boldsymbol{\epsilon}$ and the stiffness tensor $\mathbf{C}$ contain a pair of complementary jump discontinuities, so that the product stress tensor $\boldsymbol{\sigma}$ is continuous across any material boundaries. To ensure numerical convergence, Fourier series with complementary jump discontinuities are multiplied with the inverse rule [20,21,32]:

$$\sum_{\mathbf{G}}\left\{\sum_{\mathbf{G}'}\left[\frac{1}{C_{pqrs}}\right]_N^{-1}(\mathbf{G},\mathbf{G}')\epsilon_{rs}(\mathbf{G}')\right\}\exp(i\mathbf{G}\cdot\mathbf{r}) \to \sigma_{pq}(x), \tag{A5}$$

where the matrix denoted as $[1/C_{pqrs}]$ has matrix elements given by $[1/C_{pqrs}](\mathbf{G},\mathbf{G}') = (1/C_{pqrs})(\mathbf{G}-\mathbf{G}')$. The subscript $_N$ denote the relevant plane wave expansion truncation. The superscript $^{-1}$ represents matrix inversion, assuming the matrix is nonsingular:

$$\sum_{\mathbf{G}'}\left[\frac{1}{C_{pqrs}}\right]_N^{-1}(\mathbf{G},\mathbf{G}')\left[\frac{1}{C_{pqrs}}\right]_N(\mathbf{G}',\mathbf{G}'') = \delta_{\mathbf{G},\mathbf{G}''}, \tag{A6}$$

where δ_{ij} is the Kronecker delta symbol.

In our two-dimensional elastic composite consisting of linear isotropic materials, the relevant nonvanishing components are $C_{1122} = C_{2211} = \lambda$, $C_{1212} = C_{2121} = C_{3131} = C_{3232} = 2\mu$, $C_{1111} = C_{2222} = \lambda + 2\mu$. For notational convenience, the matrices $\boldsymbol{\Lambda}^{\text{inv}}$, $\boldsymbol{M}^{\text{inv}}$, and $\boldsymbol{N}^{\text{inv}}$ are introduced, with their elements, respectively, defined by

$$\Lambda^{\text{inv}}_{\mathbf{G},\mathbf{G}'} = \left[\frac{1}{C_{1122}}\right]_N^{-1}(\mathbf{G},\mathbf{G}'), \tag{A7a}$$

$$M^{\text{inv}}_{\mathbf{G},\mathbf{G}'} = \frac{1}{2}\left[\frac{1}{C_{1212}}\right]_N^{-1}(\mathbf{G},\mathbf{G}'), \tag{A7b}$$

$$N^{\text{inv}}_{\mathbf{G},\mathbf{G}'} = \left[\frac{1}{C_{1111}}\right]_N^{-1}(\mathbf{G},\mathbf{G}'). \tag{A7c}$$

Substituting the Bloch wave expansion (20) into the dynamical equation of the out-of-plane displacement field (21), and manipulating the product of the stiffness tensor and the strain tensor elements by the preceding inverse rule (A5), we obtain an eigenvalue equation governing the out-of-plane motion:

$$\sum_{\mathbf{G}'}\left[(\mathbf{K}+\mathbf{G})\cdot(\mathbf{K}+\mathbf{G}')M^{\text{inv}}_{\mathbf{G},\mathbf{G}'} - \omega_{\mathbf{K}}^2\rho(\mathbf{G}-\mathbf{G}')\right]\mathbf{u}_{z,\mathbf{K}}(\mathbf{G}') = 0, \tag{A8}$$

where the eigenvectors $\mathbf{u}_{z,\mathbf{K}}(\mathbf{G})$ correspond to the out-of-plane acoustic bands $\omega_{\mathbf{K}}$. Under the plane wave truncation $N = 10$, there are $2N+1 = 21$ plane waves per direction, and a total of $(2N+1)^2 = 441$ are incorporated in the two-dimensional reciprocal space. The underlying matrix is 441×441 in size.

Similarly, the Bloch wave expansion (20) is substituted into the dynamical equations of the in-plane displacement fields (22) and (23). Using the inverse rule (A5) for the Fourier series product of the stiffness tensor and strain tensor components, we obtain

$$\sum_{\mathbf{G}'}\left[\begin{pmatrix} D_{11}(\mathbf{G},\mathbf{G}') & D_{12}(\mathbf{G},\mathbf{G}') \\ D_{21}(\mathbf{G},\mathbf{G}') & D_{22}(\mathbf{G},\mathbf{G}') \end{pmatrix} - \omega_{\mathbf{K}}^2\begin{pmatrix} \rho(\mathbf{G}-\mathbf{G}') & 0 \\ 0 & \rho(\mathbf{G}-\mathbf{G}') \end{pmatrix}\right]\begin{pmatrix} \mathbf{u}_{x,\mathbf{K}}(\mathbf{G}') \\ \mathbf{u}_{y,\mathbf{K}}(\mathbf{G}') \end{pmatrix} = 0, \tag{A9}$$

where the elements of the dynamical matrix $\mathbf{D}(\mathbf{G},\mathbf{G}')$ are

$$D_{11}(\mathbf{G},\mathbf{G}') = N^{\text{inv}}_{\mathbf{G},\mathbf{G}'}(K_x+G_x)(K_x+G'_x) + M^{\text{inv}}_{\mathbf{G},\mathbf{G}'}(K_y+G_y)(K_y+G'_y), \tag{A10a}$$

$$D_{12}(\mathbf{G},\mathbf{G}') = \Lambda^{\text{inv}}_{\mathbf{G},\mathbf{G}'}(K_x+G_x)(K_y+G'_y) + M^{\text{inv}}_{\mathbf{G},\mathbf{G}'}(K_y+G_y)(K_x+G'_x), \tag{A10b}$$

$$D_{21}(\mathbf{G},\mathbf{G}') = \Lambda^{\text{inv}}_{\mathbf{G},\mathbf{G}'}(K_y+G_y)(K_x+G'_x) + M^{\text{inv}}_{\mathbf{G},\mathbf{G}'}(K_x+G_x)(K_y+G'_y), \tag{A10c}$$

$$D_{22}(\mathbf{G},\mathbf{G}') = N^{\text{inv}}_{\mathbf{G},\mathbf{G}'}(K_y+G_y)(K_y+G'_y) + M^{\text{inv}}_{\mathbf{G},\mathbf{G}'}(K_x+G_x)(K_x+G'_x). \tag{A10d}$$

Eigenvectors of the form of $(\mathbf{u}_{x,\mathbf{K}}(\mathbf{G}), \mathbf{u}_{y,\mathbf{K}}(\mathbf{G}))$ correspond to the in-plane acoustic bands $\omega_{\mathbf{K}}$. Under the plane wave truncation $N = 10$, $(2N+1)^2 = 441$ plane waves are incorporated. For each pair of reciprocal lattice vectors $\{\mathbf{G}, \mathbf{G}'\}$, the interaction is given by a 2×2 block dynamical matrix, $\mathbf{D}(\mathbf{G}, \mathbf{G}')$, so that the full matrix is 882×882 in size.

APPENDIX B: RCSA OF IN-PLANE TRANSLATION

In this Appendix, we express the forces acting on the cellulose shell and the steel core in terms of their displacements and the mechanical parameters of the interstitial foam. We start by evaluating the nonvanishing elements of the symmetric elastic strain tensor from the in-plane displacement profile in (42):

$$\epsilon_{ss} = \frac{\partial u_s}{\partial s} = \frac{dc_s}{ds}\cos\phi, \tag{B1a}$$

$$\epsilon_{\phi\phi} = \frac{1}{s}\left(\frac{\partial u_\phi}{\partial \phi} + u_s\right) = \left(\frac{c_s + c_\phi}{s}\right)\cos\phi, \tag{B1b}$$

$$\epsilon_{\phi s} = \epsilon_{s\phi} = \frac{1}{2}\left(\frac{1}{s}\frac{\partial u_s}{\partial \phi} + \frac{\partial u_\phi}{\partial s} - \frac{u_\phi}{s}\right) = \frac{1}{2}\left(\frac{dc_\phi}{ds} - \frac{c_s + c_\phi}{s}\right)\sin\phi. \tag{B1c}$$

Using the generalized Hooke's law (16) for linear isotropic solids, we determine the relevant components of the symmetric stress tensor:

$$\sigma_{ss} = \left[\lambda\left(\frac{dc_s}{ds} + \frac{c_s + c_\phi}{s}\right) + 2\mu\frac{dc_s}{ds}\right]\cos\phi, \tag{B2a}$$

$$\sigma_{\phi\phi} = \lambda\left(\frac{dc_s}{ds} + \frac{c_s + c_\phi}{s}\right)\cos\phi + 2\mu\left(\frac{c_s + c_\phi}{s}\right)\cos\phi, \tag{B2b}$$

$$\sigma_{\phi s} = \sigma_{s\phi} = 2\mu\epsilon_{s\phi} = \mu\left(\frac{dc_\phi}{ds} - \frac{c_s + c_\phi}{s}\right)\sin\phi. \tag{B2c}$$

In the absence of an external body force at elastostatic equilibrium, the stress tensor is divergence-free, $\nabla \cdot \boldsymbol{\sigma} = \mathbf{0}$:

$$\frac{\partial \sigma_{ss}}{\partial s} + \frac{1}{s}\frac{\partial \sigma_{s\phi}}{\partial \phi} + \frac{1}{s}(\sigma_{ss} - \sigma_{\phi\phi}) = 0, \tag{B3a}$$

$$\frac{\partial \sigma_{s\phi}}{\partial s} + \frac{1}{s}\frac{\partial \sigma_{\phi\phi}}{\partial \phi} + \frac{2\sigma_{s\phi}}{s} = 0. \tag{B3b}$$

Substituting Eqs. (B2a) to (B2c) into Eqs. (B3a) and (B3b) yields a set of coupled dynamical equations for elastic response:

$$(\lambda + 2\mu)\frac{d^2c_s}{ds^2} + \left(\frac{\lambda + 2\mu}{s}\right)\frac{dc_s}{ds} + \left(\frac{\lambda + \mu}{s}\right)\frac{dc_\phi}{ds} - \frac{\lambda + 3\mu}{s^2}(c_s + c_\phi) = 0, \tag{B4a}$$

$$\mu\frac{d^2c_\phi}{ds^2} + \frac{\mu}{s}\frac{dc_\phi}{ds} - \left(\frac{\lambda + \mu}{s}\right)\frac{dc_s}{ds} - \frac{\lambda + 3\mu}{s^2}(c_s + c_\phi) = 0. \tag{B4b}$$

Four linearly independent solutions of this homogeneous system of two coupled second-order differential equations can be verified by direct substitution:

$$(c_s(s), c_\phi(s)) = (1, -1), \tag{B5a}$$

$$(c_s(s), c_\phi(s)) = \ln s\,(1, -1) - \frac{\lambda + \mu}{2(\lambda + 3\mu)}(1, 1), \tag{B5b}$$

$$(c_s(s), c_\phi(s)) = \frac{1}{s^2}\,(1, 1), \tag{B5c}$$

$$(c_s(s), c_\phi(s)) = s^2(\lambda - \mu, -3\lambda - 5\mu). \tag{B5d}$$

The desired solution satisfying the boundary conditions (43a) to (43d) are formed by proper linear combination of the four basis solutions:

$$c_s(s) = \frac{1}{\Delta}\left[\frac{F_1}{s^2} + F_2(\lambda - \mu)s^2 + F_3 + F_4(\ln s - \eta)\right], \tag{B6a}$$

$$c_\phi(s) = \frac{1}{\Delta}\left[\frac{F_1}{s^2} - F_2(3\lambda + 5\mu)s^2 - F_3 - F_4(\ln s + \eta)\right], \tag{B6b}$$

where Δ, η, and F_i are algebraic expressions of the material parameters of the foam, the core displacement X_c, and the shell displacement X_s of the resonant unit:

$$\Delta \equiv (\lambda + 3\mu)^2\left(R_1^2 + R_2^2\right)\ln R_2/R_1 - (\lambda + \mu)^2\left(R_2^2 - R_1^2\right), \tag{B7a}$$

$$\eta \equiv \frac{\lambda + \mu}{2(\lambda + 3\mu)}, \tag{B7b}$$

$$F_1 \equiv \frac{1}{2}(\lambda + \mu)(\lambda + 3\mu)R_1^2R_2^2(X_s - X_c), \tag{B7c}$$

$$F_2 \equiv -\frac{1}{2}(\lambda + \mu)(X_s - X_c), \tag{B7d}$$

$$F_3 \equiv (\lambda + \mu)^2\left(R_1^2X_s - R_2^2X_c\right) - (\lambda + 3\mu)^2\left(R_1^2 + R_2^2\right)(X_s \ln R_1 - X_c \ln R_2), \tag{B7e}$$

$$F_4 \equiv (\lambda + 3\mu)^2\left(R_1^2 + R_2^2\right)(X_s - X_c). \tag{B7f}$$

The force per unit length acting on the steel core, $\mathbf{f}_{c,x}$, and that on the cellulose shell, $\mathbf{f}_{s,x}$, are determined from the stress tensor:

$$\begin{aligned}\mathbf{f}_{c,x} &= \oint_{\{s=R_1\}} \boldsymbol{\sigma}\cdot\hat{\mathbf{n}}\, dl = \int_0^{2\pi} (\sigma_{ss}\,\hat{\mathbf{s}} + \sigma_{\phi s}\,\hat{\boldsymbol{\phi}})\, R_1 d\phi \\ &= \int_0^{2\pi} [(\sigma_{ss}\cos\phi - \sigma_{\phi s}\sin\phi)\,\hat{\mathbf{x}} + (\sigma_{ss}\sin\phi - \sigma_{\phi s}\cos\phi)\,\hat{\mathbf{y}}]\, R_1 d\phi \\ &= \frac{4\pi\mu F_4}{\Delta}\left(\frac{\lambda + 2\mu}{\lambda + 3\mu}\right)\hat{\mathbf{x}},\end{aligned} \tag{B8}$$

$$\mathbf{f}_{s,x} = \oint_{\{s=R_2\}} \boldsymbol{\sigma}\cdot\hat{\mathbf{n}}\, dl = -\mathbf{f}_{c,x}. \tag{B9}$$

The required stress tensor components are calculated by substituting Eqs. (B6a) and (B6b) into (B2a) and (B2c):

$$\sigma_{ss}(s,\phi) = -\frac{2\mu\cos\phi}{\Delta}\left[\frac{2F_1}{s^3} + 2F_2(\lambda + \mu)s - \left(\frac{2\lambda + 3\mu}{\lambda + 3\mu}\right)\frac{F_4}{s}\right], \tag{B10a}$$

$$\sigma_{s\phi}(s,\phi) = -\frac{2\mu\sin\phi}{\Delta}\left[\frac{2F_1}{s^3} + 2F_2(\lambda + \mu)s + \left(\frac{\mu}{\lambda + 3\mu}\right)\frac{F_4}{s}\right]. \tag{B10b}$$

We remark that our RCSA results are low-frequency analytic solutions of a model proposed by Lui *et al.* [14] without requiring a full-wave treatment. Wave propagation in the solid foam medium can be decomposed into compression and shear waves. The longitudinal compression wave propagates at the speed $c_l = \sqrt{(\lambda + 2\mu)/\rho}$, while the transverse shear wave propagates at the speed $c_t = \sqrt{\mu/\rho}$. When only the relative translation between the rigid cellulose shell and the rigid steel core is considered, only the $n = 1$ terms are nonvanishing in a partial wave expansion of the displacement field. The displacement can be expressed in terms of the potential functions Φ_c and Φ_s:

$$\mathbf{u} = \nabla\Phi_c + \nabla\times(\Phi_s\hat{\mathbf{z}}). \tag{B11}$$

The potential functions of the compression wave and the shear wave are solutions of the scalar wave equation in cylindrical coordinates:

$$\Phi_c(s,\phi,t) = \left[p_1J_1\left(\frac{\omega s}{c_l}\right) + p_2K_1\left(\frac{\omega s}{c_l}\right)\right]\cos\phi\; e^{-i\omega t}, \tag{B12}$$

$$\Phi_s(s,\phi,t) = \left[p_3J_1\left(\frac{\omega s}{c_t}\right) + p_4K_1\left(\frac{\omega s}{c_t}\right)\right]\sin\phi\; e^{-i\omega t}. \tag{B13}$$

Here J_1 and K_1 are Bessel functions of the first kind and the second kind, and the constants p_1, p_2, p_3 and p_4 are determined by the boundary conditions. When the wavelength of sound is much longer than the relevant dimensions of the resonant unit (low-frequency limit), the Bessel functions can be expanded for small values of their arguments:

$$J_1(z) \approx \frac{z}{2} - \frac{z^3}{16} + O[z^5], \tag{B14}$$

$$K_1(z) \approx \frac{1}{z} + \frac{z}{4}\left(2\gamma - 1 + 2\ln\frac{z}{2}\right) + O[z^3], \tag{B15}$$

where $\gamma \approx 0.5772$ is the Euler-Mascheroni constant. Using Eq. (B11), we recover terms involving spatial dependence of the form of $1/s^2$, 1, $\ln s$, and s^2 in agreement with our basis solutions in Eq. (B5a) to (B5d). Unlike the partial wave analysis of Lui *et al.* [14], our RCSA provides closed form algebraic expressions of the effective densities. For the low-frequency bands of our phononic crystal, it is reasonable to neglect the wave propagation in the interstitial foam within the resonant unit. A full-wave treatment is needed at higher frequencies, when the wavelength of sound is comparable to the size of the resonant unit.

APPENDIX C: RCSA OF IN-PLANE ROTATION

When the steel core rotates relative to the cellulose shell, the annular layer of elastic interstitial foam provides a restoring torque. In this Appendix, we express the torques acting on the core and the shell in terms of the angles of in-plane rotation of the approximate rigid bodies and the material parameters of the foam in the long wavelength regime. This analysis utilizes the constitutive relation between strain and stress for the divergence-free stress tensor field under elastostatic equilibrium.

For the rotationally symmetric displacement profile (50), the only nonvanishing components of the symmetric strain tensor $\boldsymbol{\epsilon}$ are $\epsilon_{\phi s}$ and $\epsilon_{s\phi}$:

$$\epsilon_{\phi s} = \epsilon_{s\phi} = \frac{1}{2}\left(\frac{1}{s}\frac{\partial u_s}{\partial \phi} + \frac{\partial u_\phi}{\partial s} - \frac{u_\phi}{s}\right) = \frac{1}{2}\left(\frac{db}{ds} - \frac{b}{s}\right). \tag{C1}$$

The generalized Hooke's law (16) for linear isotropic solids reveals that the only nonvanishing components of the symmetric stress tensor $\boldsymbol{\sigma}$ are $\sigma_{\phi s}$ and $\sigma_{s\phi}$:

$$\sigma_{\phi s} = \sigma_{s\phi} = 2\mu\epsilon_{s\phi} = \mu\left(\frac{db}{ds} - \frac{b}{s}\right). \tag{C2}$$

In the absence of an external body force, the stress tensor is divergence-free, $\boldsymbol{\nabla}\cdot\boldsymbol{\sigma} = \mathbf{0}$:

$$\frac{\partial \sigma_{s\phi}}{\partial s} + \frac{1}{s}\frac{\partial \sigma_{\phi\phi}}{\partial \phi} + \frac{2\sigma_{s\phi}}{s} = 0. \tag{C3}$$

Substituting Eq. (C2) into Eq. (C3), we obtain

$$\mu\left(\frac{d^2b}{ds^2} + \frac{1}{s}\frac{db}{ds} - \frac{b}{s^2}\right) = 0. \tag{C4}$$

Solving Eq. (C4) by a standard power-law ansatz, and imposing the boundary conditions (51a) and (51b), we obtain

$$b(s) = \frac{E(\Psi_c - \Psi_s)}{s} + \frac{R_2^2\Psi_s - R_1^2\Psi_c}{R_2^2 - R_1^2}s, \tag{C5}$$

$$\sigma_{\phi s} = \sigma_{s\phi} = \mu\left(\frac{db}{ds} - \frac{b}{s}\right) = 2\mu E\frac{\Psi_s - \Psi_c}{s^2}, \tag{C6}$$

where $E = R_1^2R_2^2/(R_2^2 - R_1^2)$. The torque per unit length acting on the steel core, $\boldsymbol{\tau}_c$, and that on the cellulose shell, $\boldsymbol{\tau}_c$, are determined from the stress tensor:

$$\boldsymbol{\tau}_c = \oint_{\{s=R_1\}} \mathbf{r}\times(\boldsymbol{\sigma}\cdot\hat{\mathbf{n}})\,dl = 4\pi\mu E(\Psi_s - \Psi_c)\hat{\mathbf{z}}, \tag{C7}$$

$$\boldsymbol{\tau}_s = \oint_{\{s=R_2\}} \mathbf{r}\times(\boldsymbol{\sigma}\cdot\hat{\mathbf{n}})\,dl = 4\pi\mu E(\Psi_c - \Psi_s)\hat{\mathbf{z}}, \tag{C8}$$

where $\hat{\mathbf{n}}$ denotes a unit inward normal vector on the boundary. $\boldsymbol{\tau}_c + \boldsymbol{\tau}_s = \mathbf{0}$, as required by Newton's third law.

[1] S. John, Phys. Rev. Lett. **58**, 2486 (1987).
[2] E. Yablonovitch, Phys. Rev. Lett. **58**, 2059 (1987).
[3] S. John and J. Wang, Phys. Rev. Lett. **64**, 2418 (1990).
[4] S. Bhattacharya and S. John, APL Photonics **5**, 020902 (2020).
[5] S. John, H. Sompolinsky, and M. J. Stephen, Phys. Rev. B **27**, 5592 (1983).
[6] S. John and M. J. Stephen, Phys. Rev. B **28**, 6358 (1983).
[7] M. S. Kushwaha, P. Halevi, L. Dobrzynski, and B. Djafari-Rouhani, Phys. Rev. Lett. **71**, 2022 (1993).
[8] M. S. Kushwaha, P. Halevi, G. Martínez, L. Dobrzynski, and B. Djafari-Rouhani, Phys. Rev. B **49**, 2313 (1994).
[9] F. R. Montero de Espinosa, E. Jiménez, and M. Torres, Phys. Rev. Lett. **80**, 1208 (1998).
[10] J. O. Vasseur, P. A. Deymier, B. Chenni, B. Djafari-Rouhani, L. Dobrzynski, and D. Prevost, Phys. Rev. Lett. **86**, 3012 (2001).
[11] J. V. Sánchez-Pérez, D. Caballero, R. Mártinez-Sala, C. Rubio, J. Sánchez-Dehesa, F. Meseguer, J. Llinares, and F. Gálvez, Phys. Rev. Lett. **80**, 5325 (1998).
[12] H. M. Ledbetter, N. V. Frederick, and M. W. Austin, J. Appl. Phys. **51**, 305 (1980).
[13] Z. Liu, X. Zhang, Y. Mao, Y. Y. Zhu, Z. Yang, C. T. Chan, and P. Sheng, Science **289**, 1734 (2000).
[14] Z. Liu, C. T. Chan, and P. Sheng, Phys. Rev. B **71**, 014103 (2005).
[15] A. Colombi, P. Roux, S. Guenneau, and M. Rupin, J. Acoust. Soc. Am. **137**, 1783 (2015).
[16] M. Dubois, E. Bossy, S. Enoch, S. Guenneau, G. Lerosey, and P. Sebbah, Phys. Rev. Lett. **114**, 013902 (2015).
[17] O. Toader and S. John, Phys. Rev. E **70**, 046605 (2004).
[18] Y. Pennec, J. O. Vasseur, B. Djafari-Rouhani, L. Dobrzyński, and P. A. Deymier, Surf. Sci. Rep. **65**, 229 (2010).
[19] S. Nemat-Nasser, J. R. Willis, A. Srivastava, and A. V. Amirkhizi, Phys. Rev. B **83**, 104103 (2011).
[20] P. Lalanne, Phys. Rev. B **58**, 9801 (1998).
[21] Y. Cao, Z. Hou, and Y. Liu, Phys. Lett. A **327**, 247 (2004).
[22] M. G. Baboly, Y. Soliman, M. F. Su, C. M. Reinke, Z. C. Leseman, and I. El-Kady, Photon. Nanostruct. **12**, 487 (2014).
[23] J. Li and C. T. Chan, Phys. Rev. E **70**, 055602(R) (2004).
[24] D. Torrent and J. Sánchez-Dehesa, New J. Phys. **13**, 093018 (2011).
[25] A. N. Norris, A. L. Shuvalov, and A. A. Kutsenko, Proc. R. Soc. London A **468**, 1629 (2012).
[26] D. Torrent, Y. Pennec, and B. Djafari-Rouhani, Phys. Rev. B **92**, 174110 (2015).
[27] G. Ma and P. Sheng, Sci. Adv. **2**, e1501595 (2016).
[28] Z. Yang, J. Mei, M. Yang, N. H. Chan, and P. Sheng, Phys. Rev. Lett. **101**, 204301 (2008).
[29] L. Landau, E. Lifshitz, A. Kosevich, J. Sykes, L. Pitaevskii, and W. Reid, *Theory of Elasticity*, Vol. 7, Course of Theoretical Physics (Elsevier Science, Oxford, 1986).
[30] J. Carvill, *Mechanical Engineer's Data Handbook* (Elsevier Butterworth Heinemann, Oxford, 1993).

[31] B. Moore, T. Jaglinski, D. Stone, and R. Lakes, Cell. Polym. **26**, 1 (2007).
[32] L. Li, J. Opt. Soc. Am. A **13**, 1870 (1996).
[33] H. C. Wilcox, J. Elast. **9**, 221 (1979).
[34] A. Taflove, *Advances in Computational Electrodynamics: The Finite-Difference Time-Domain Method* (Artech House, Norwood, MA, 2000).
[35] A. Chutinan and S. John, Phys. Rev. A **78**, 023825 (2008).